Theoretical Study of the Binding of Metal Thiocyanate Complexes to Gold Surfaces

Kantaro Tazoe

University of Oxford

New College

A thesis submitted for the degree of

Master of Science



Abstract

This thesis presents a density functional theory investigation into the nature of NCS based linear and octahedral complexes in the gas-phase, as well as the surface effect of those on an Au(111) substrate. In chapter 3, we start to explore very simple linear complexes of a proton and transition metal centers (M = Cu^+, Ag^+, Au^+). In addition, a *trans* ligand (L = NH_3, CN^-) is attached in a linear geometry in terms of the stability of N- and S- coordinated isomers and the shift of resonance structure of NCS ligand. After the geometry optimization, we move to the surface effect caused by Au(111) surface when those complexes chemisorb on the substrate in chapter 4. Three possible chemisorption sites (on-top, side-on, hollow) are examined to measure structural and electrical changes on those linear complexes. The calculation of single molecules is done by ADF software and those with Au surface are done by periodic system in VASP software.

In chapter 5, we explore octahedral complexes of Fe(II), mainly $Fe(II)(phen)_2(NCS)_2$ with two spin crossover states (singlet and quintet) using an array of different functionals (PBE, OPBE, B3LYP, B3LYP*, PBE0, s12H). It is known that the exchange energy of the functional hugely effects the stability of a particular spin state and we explore those in comparison with structural properties from experimental and theoretical work. In the next section, we focus on the chemisorption of those optimised structures on Au(111) surface. As examined with linear complexes, structural and electrical properties (energy, bond length, spin density) are thoroughly analyzed, and finally we explore *U* values (*U* = 0.0, 1.5, 2.5, 3.5) which effects the exchange energy of the periodic calculation.

Acknowledgement

I would like to thank Professor John McGrady for his supervision and guidance during my M.Sc., not only for his academic support, but also our constant discussion and advice about my career and college life. I have been in touch with various fields of chemistry in my research from physical chemistry to inorganic chemistry. This could not have been achieved without his supervision.

I could also count on the support of my colleagues from Professor McGrady's group. I thank the sincere help from Vaida Arcisauskaite, and having enjoyable conversation and scientific discussion with Karrar Ameed, Andy Zeng, Xiao Jin and all others.

Invaluable time spent was with friends in New College Rugby Football Club and Oxford University Athletic Club. I have enjoyed and learnt the aspects of culture and sports from those activities and socials.

My previous supervisors from Kyushu, Professor Aleksandar Staykov has been in touch with me since the very first day I arrived in Oxford, offering constant advice and highly valuable scientific background knowledge. In addition, he has been an outstanding mentor even before I came to the UK.

A special acknowledgement goes to my family and grandparents for getting worried about my life and hearing news in the UK. I could not have achieved this work without their support.

Author's declaration

This thesis is an account of the work carried out by the author in the Department of Chemistry, University of Oxford, under the supervision of Professor John McGrady between October 2014 and March 2017. No part of this thesis has previously been submitted for a degree in this University or elsewhere. The work of other authors has been freely drawn and is duly acknowledged in the text. A list of references is given at the end of the thesis.

Glossary of abbreviation and acronyms

ADF	Amsterdam Density Functional
B3LYP	Becke three-parameter Lee-Yang-Parr
BZ	Brillouin zone
DFT	Density Functional Theory
DZP	Double *Zeta* Polarized
EMAC	Extended Metal Atom Chain
GGA	Generalized Gradient Approximation
GTO	Gaussian Type Orbital
HF	Hartree-Fock
HOMO	Highest Occupied Molecular Orbital
LDA	Local Density Approximation
LIESST	Light-induced Excited Spin State Trapping
LSDA	Local Spin Density Approximation
LUMO	Lowest Unoccupied Molecular Orbital
MOSFET	Metal-Oxide Semiconductor Field Effect Transistor
PBE	Perdew–Burke-Ernzerhof
Phen	Phenanthroline
SAM	Self-Assembled Monolayer
SCF	Self-Consistent Field
SCO	Spin Crossover
STM	Scanning Tunneling Microscope
STO	Slater Type Orbital
TZP	Triple *Zeta* Polarized
VASP	Vienna Ab-initio Simulation Package

Table of contents

1. Introduction 9

1.1. Miniaturisation of MOSFET and its limitations 9

1.2. History and Applications of Single Molecular Electronics 10

1.3. Molecular junctions formed using NCS ligands 13

2. Methodology 19

2.1. Elementary concepts of quantum mechanics 19

2.2. Hartree-Fock approximation 22

2.3. Density Functional Theory 23

2.4. The local density approximation (LDA) 25

2.5. The generalised gradient approximation (GGA) 25

2.6. Hybrid functionals 26

2.7. The Kohn-Sham approach to DFT 27

2.8. Localised basis sets 27

2.9. Amsterdam Density Functional (ADF) software 29

2.10. Cluster and Periodic ab-initio calculations 29

2.11. Plane wave and LCAO basis sets 29

2.12. Brillouin zone sampling 30

2.13. Pseudopotential 30

3. Structure and property of L-M-NCS complexes (M = H^+, Au^+, Ag^+, Cu^+) with ligands (L = NH_3, CN^-) 32

3.1. Introduction 32

3.2. H-NCS and its conjugate base, NCS^- 34

3.3. M-NCS, M = Cu^+, Ag^+ and Au^+ 37

3.4. Potential energy surface of L-M-NCS (L = NH_3 and CN^-), M = Cu^+, Ag^+ and Au^+ 41

4. Bonding of NCS complexes to a gold (111) surface 47

4.1 Introduction 47

4.2. Convergence test 49

4.3. Surface effects on the bonding of H-NCS on Au (111) 51

4.4. Surface effects of binding of (Cu^+, Ag^+, Au^+)-NCS to Au (111) 52

4.5. Surface effects of binding of (NH_3, CN^-)-(Cu^+, Ag^+, Au^+)-NCS to Au(111) surface 54
4.6. Summary 58

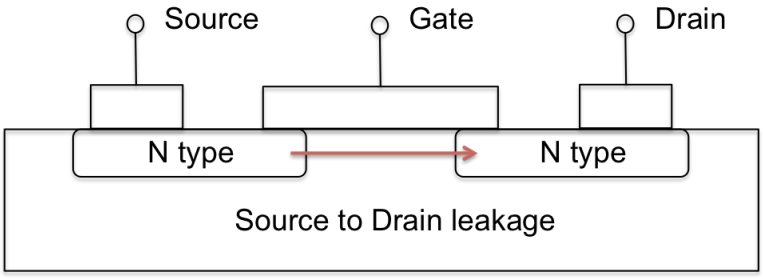
5. Structure and properties of spin crossover complexes of Fe(II): Fe(II)$(phen)_2(NCS)_2$. 59
5-1. Introduction 59
5.2. Gas-phase studies on spin crossover in Fe(II)$(phen)_2(NCS)_2$ 61
5.3. Gas-phase studies on spin crossover in Fe(II)$(diimine)_2(NCS)_2$ 64
5.4 Influence of surface binding on the spin-crossover in Fe(II)$(phen)_2(NCS)_2$ 66
5.5. Summary 72

6. Conclusion 73

7. References 75

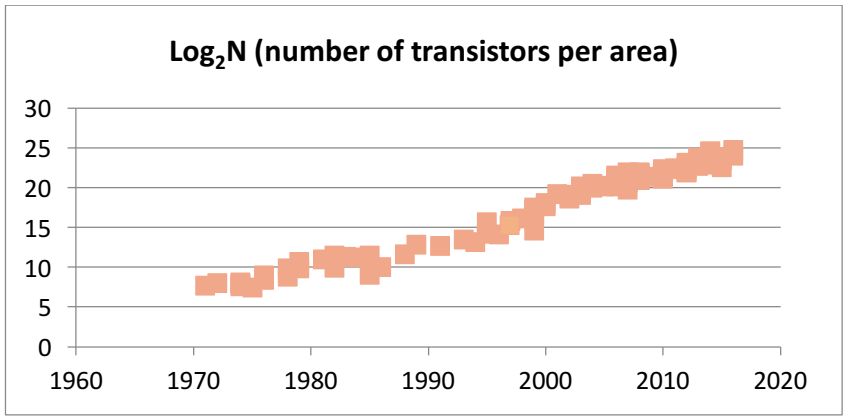
1. Introduction

1.1. Miniaturisation of MOSFET and its limitations



[Figure 1.1] Schematic diagram of MOSFET device

The downsizing of semiconductor components in electronic devices has been the most important driver for the electronics industry for over 50 years. The MOSFET (Metal-Oxide-Semiconductor Field Effect Transistor), invented by Dawon Kahng in Bell Telephone Laboratories in 1960[1], is a fundamental component of digital integrated circuits such as microprocessors and memory devices, which contain millions of MOSFET-type transistors (Figure 1.1). A MOSFET-type transistor consists of three terminals with source, gate and drain. The bulk is made from a p-type semiconductor (boron doped silicon) attached to the gate and two n-type semiconductor (phosphine doped silicon) regions are deposited to act as the source and drain. The depletion region, which presents a barrier to current flow from n-type bulk to p-type regions, is created by a p-n junction. When a positive voltage is applied to the gate, negatively charged electrons are attracted to the surface of the p-type bulk resulting in current flow.



[Figure 1.2] Number of transistors per area (on a logarithmic scale), following Moore's law

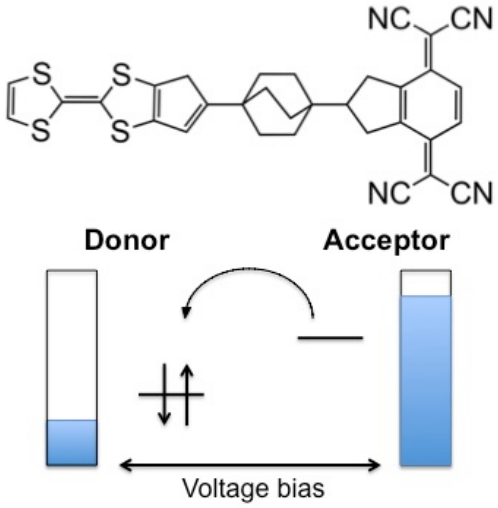
Five years after the discovery of MOSFET, in 1965, G. E. Moore of Intel anticipated that the number of transistors that can be placed in cutting edge integrated circuit chips would double approximately every two years, based on the rapid progress made from 1959 to 1965.[2] This prediction has proved to be remarkably accurate over the past 50 years (Figure 1.2), over which time semiconductor components have shrunk dramatically and have reached dimensions of 10 nm.[3] Nevertheless, the rate of progress is slowing, and in 2015 Intel revised Moore's prediction down to every two and a half years.

Further innovation and progress in the semiconductor industry will undoubtedly sustain MOSFET technology in the near future, but further downsizing results in increased device variability and the technology will eventually face fundamental limitations, such as source-to-drain and gate-to-oxide leakage. These leakages allow electron tunnelling without any operation of the voltage on the gate. In addition, further miniaturization of electronic components presents manufacturing challenges: it becomes increasingly difficult to control the position of small numbers of atoms in a top-down building approach. As a result, a paradigm shift is required from the traditional top-down approaches to bottom-up building of molecular components into electronic circuits.[4]

1.2. History and Applications of Single Molecular Electronics

Single molecule electronics presents one possible solution to address the inherent limitations of MOSFET technology because a single molecule constitutes the smallest stable structure possible, the ultimate goal for miniaturization of electronic circuits. The reduced size of small molecules compared to current silicon-based components (between 1 to 10 nm) could lead to a higher packing density with subsequent advantages in cost, efficiency and power dissipation. Moreover, one can exploit specific intermolecular interactions to form structures by taking advantage of the self-assembly properties of molecules.[5] A single molecule attached to two electrodes is a basic component in molecular electronics, and electron transport through the molecule may be controlled electrically, magnetically and optically, leading to various potential device applications including switches, diodes and transistors. In addition, intriguing

quantum effects in molecular electronics have attracted the attention of scientist in various disciplines in recent years.[6, 7, 8]

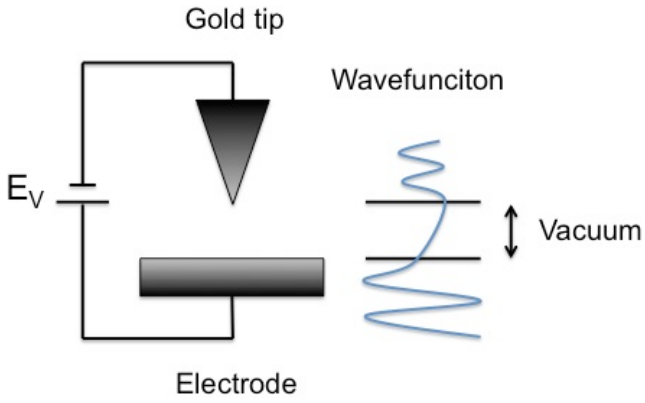


[Figure 1.3] Schematic diagram of Aviram-Ratner model

The field of molecular electronics can be traced back to studies conducted by B. Mann & H. Kuhn in 1971,[9] who measured conductivity through monolayers of cadmium salts of fatty acid. These measurements showed that the conductivity decreased exponentially with layer thickness, revealing electron tunnelling through the organic monolayer. The first theoretical discussion of electron transport through a single molecule was reported in 1974 by A. Aviram & M. Ratner,[10, 11] where they described how a modified charge-transfer salt could operate as a traditional diode in an electrical circuit (Figure 1.3). They suggested that electron-donating and electron-withdrawing substituents confer N-type and P-type character, respectively, on an organic framework. This showed that the lowest unoccupied molecular orbital (LUMO) and highest occupied molecular orbital (HOMO) can be aligned in such a way that electronic conduction is possible only in one direction, making it function like a molecular diode. That was in fact the beginning of many theoretical approaches, which have led to the non-equilibrium Green's function approaches that are generally applied to calculate electron transport properties in single molecules.[12]

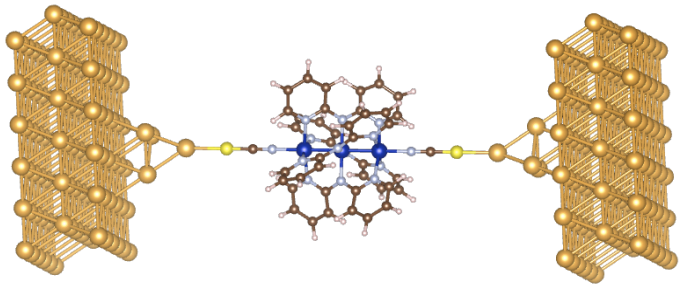
From an experimental perspective, however, the greatest challenge in the field is to attach a molecule to an electrode surface and measure its electron transport properties in a reproducible manner. In the 1980s, perhaps the most important

advance in molecular electronics occurred with the development of the Scanning Tunnelling Microscope (STM), produced by G. Binning & H. Rohrer in IBM Zuric.[13] This technique successfully yielded a true three-dimensional topography of surfaces on an atomic scale by using the vacuum tunnelling effect (Figure 1.4). This technique has provided a realistic way to address single molecules and has given many important insights into transport properties.[14] The biggest problems faced by experimentalists is that the results inevitably show large stochastic fluctuations due to essentially random conformational changes and detachment of the molecules tethered to the gold surface.[15] This final point emphasises the importance of understanding the chemisorption of molecules on the electrode surface, and the impact of variations therein on conductance. This is the motivation for the present thesis.



[Figure 1.4] Schematic diagram of vacuum tunnelling effect on STM

1.3. Molecular junctions formed using NCS ligands

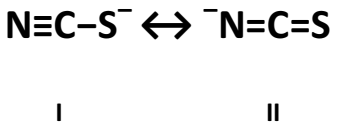


[Figure 1.5] EMACs: extended metal atom chain, consists of a chain of 3 Co^{2+} atoms surrounded helically with pyridylamine, and with thiocyanate ligands

A very common strategy in molecular electronics is to use ligands such as NCS to link the molecule, bound *via* the nitrogen donor, to a gold electrode surface *via* the sulfur donor atom. The motivation for this is simply that sulfur has a well-established affinity for gold. In many studies, it has been shown that the molecule-NCS-electrode junction is the current-limiting barrier, and so the electronic details of the M-N and S-Au bonds are clearly of some importance. As an example, Peng and co-workers have synthesised a range of Extended Metal Atom Chain (EMACs) and used NCS ligands to attach them to gold surfaces. In the 1990s the chemistry of the EMACs was developed in Peng's group at the National Taiwan University as well as by F. A. Cotton in Texas A&M.[16, 17] EMACs represent some of the smallest molecular wires, consisting of linear strings of directly bonded transition metal atoms surrounded helically by four long organic ligands (Figure 1.5). The transition metal chains are typically fabricated from Cr, Co and Ni, surrounded by four organic ligands made of repeating pyridylamidos. These molecular wires bear a superficial resemblance to macroscopic wires, and this has motivated a number of studies of electron transport properties using STM. The fabrication process of depositing single molecules on the metal electrodes has been reasonably straightforward: once the core of a molecule is synthesized, the molecule is attached to the gold electrodes *via* the sulfur atom of an NCS ligand. It is assumed that the covalent bond between gold and sulfur gives rise to a robust junction. As noted above, the greatest problem in measuring conductance using STM is stochastic switching, where the chemisorption site between the sulfur-containing ligand and the gold surface

changes. This phenomenon has been observed in the context of a long chain organic molecule in a matrix of Self-Assembled Monolayer (SAM) on a gold surface, and rationalized in terms of conformational changes of the molecule.[18, 19, 20] In the experimental work on EMACs using STM measurements, similar conductance and stochastic switching has been observed with NCS ligands.[21] An additional, often unstated, assumption is that the Au-S junction is approximately the same for all molecules, because only then can attention to be placed on variations in the metal content when interpreting trends. However, it is by no means clear that the Au-S interaction is independent of the composition of the chain, because the binding of NCS to the metal *via* nitrogen may influence the binding of the sulfur donor to gold.

The potential nature of this influence is illustrated in Figure 1.7, where the two possible resonance structures of NCS^- are shown. In the first, the negative charge is localized on the nitrogen and there are double N=C and C=S bonds, while in the other the negative charge is localized on S, and the N-C bond is formally considered to be triple. Of course, in isolation these two resonance forms are simply limiting descriptions of a single equilibrium structure, but coordination of metal ions to either end can be interpreted in terms of physically real shifts in the balance between the two. Thus, coordination of a cation to the nitrogen end will shift the balance in favor of resonance structure I to maximize the electrostatic interaction. This will in turn reduce the negative charge on sulfur, altering its ability to bind to another atom or surface. Moreover, the shifts in balance between resonance structures I and II should be detectable through small but distinct changes in N-C and C-S bond lengths that reflect the differences in bond order. The potential for binding at one site to influence the other end is perhaps best illustrated by the so-called "azide effect", where N_3^- is known to be a much stronger bridging ligand than NCS. In N_3^-, there is a negative charge at both ends of the molecule; so, binding to one end does not have such a dramatic influence on the ability of the other to bind to a second metal.

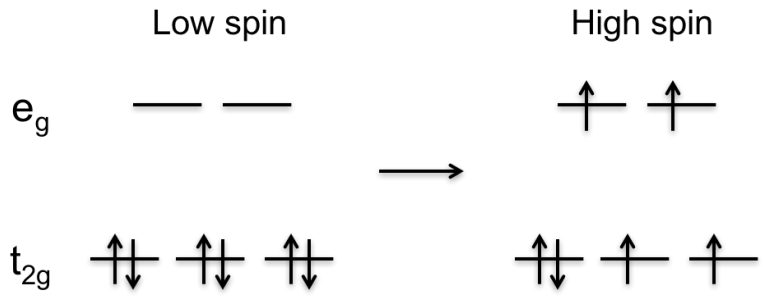


[Figure 1.6] Resonance structures of NCS

In the first section of this thesis I explore the binding of the NCS ligand to the simplest model cations, the naked d^{10} cations of group 11: Cu^+, Ag^+, Au^+ and also their NH_3 and CN^--coordinated analogue, ML. Whilst these are clearly greatly simplified models of the EMACs, they serve to establish the patterns that we explore in the second chapter on spin crossover. Transition metals with a d^{10} valence count often prefer linear coordination, with the preference increasing in order of increasing atomic number (Cu < Ag < Au) to the extent that the coordination chemistry of Au(I) is dominated by linear complexes even where tri or tetra coordinated alternatives are available. The dominant component of the M-NCS bond then comes from σ donation from the ligand's lone-pair into the empty (n+1)s atomic orbital of the metal. We anticipate that the binding of a metal at the nitrogen and the *trans* ligand effect will alter the balance between the two resonance forms shown in Figure 1.6, such that more negative charge will accumulate on the nitrogen. This, in turn, may influence the ability of the sulfur atom to bind to the gold surface. In the second part of this thesis we turn attention to spin crossover compounds, which have been attracting much interest in the molecular electronics field simply because a change in spin state induced by external stimuli such as temperature, light, pressure, solvent coordination or electric field can provide a switching mechanism between conductive and non-conductive states.[22, 23] Spin crossover is associated with d^4-d^7 electron configurations, where promotion of an electron from a t_{2g} (non-bonding) orbital to e_g (anti-bonding) orbital results in dramatic changes in the length of the M-N bonds (Figure 1.7).

The first spin crossover compound, a Fe(III) dithiocarbamate complex, was reported by Cambi *et al*. in 1931 and since then arrays of mono and poly nuclear iron complexes have been created, the majority of which contain Fe(II) d^6

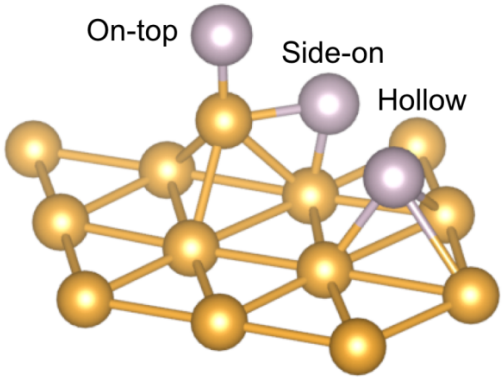
complexes with 6 nitrogen donor ligands. From a theoretical point of view, spin crossover is an extremely challenging topic because the balance between high- and low-spin forms is a subtle balance between kinetic energy, electrostatic attraction between protons and electrons and electron-electron repulsion. The high-spin configuration is stabilized by the exchange energy which reduces the repulsion between like-spin electrons, and this term differs substantially from one density functional to another. As a result, the balance between high and low-spins is also strongly influenced by the choice of the exchange-correlation functionals. In general, GGA and LDA functionals tend to overestimate the low-spin state stability, while the well-known hybrid function as B3LYP and B3LYP* give the opposite effect as hybrid functionals take a part of the exchange energy from the HF method. In the final chapter, we use a range of density functionals to explore the energetic balance between low and high spin states for a model Fe(II) complexes.



[Figure 1.7] Electron configurations of Fe(II) low and high spin states

In the second component of the chapter, a highly idealized perfect (111) gold surface is used to model chemisorption of the complexes on a surface. Once again, our focus is on understanding how changes in the spin configuration at the metal center impact on the ability of the NCS ligand to bind remotely to the gold surface *via* the sulfur atom. Equally, binding to the metal surface can alter the donor ability of the nitrogen atom, altering the high-spin/low-spin balance Alkane-thiolate SAMs adsorbed on an Au(111) surface have been studied in great detail, primarily using density functional theory. For example, recent papers by Gronbeck *et al*. from the IBM Research Laboratory explored the adsorption of methane-thiol on an Au(111) surface which was modelled by 4 layers of a 5x5

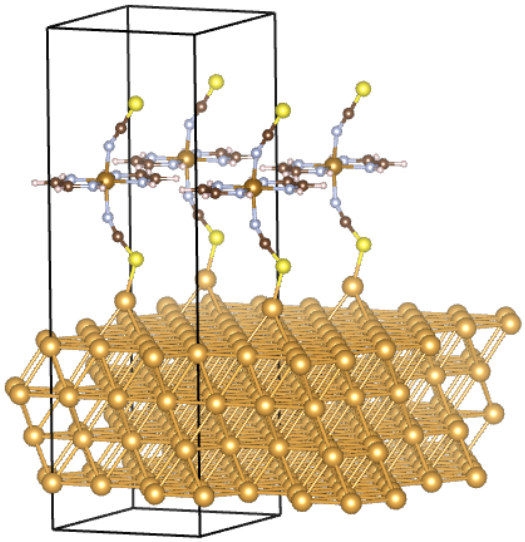
surface slab, giving reasonable agreement with experimental evidence.[24] Later, J. Gottschalck and B. Hammer explored three sulfur adsorbates, a sulfur atom, a mercapto ligand and a methyl-thiolate ligand, on an Au(111) surface.[25] It is well known that substrate binding can trigger substantial reconstructions of Au surfaces, giving a degree of roughness.[26] Those reconstructions change not only the structure of the underlying Au substrate but also affect the chemical binding between the substrate and the ligand. In order to mimic these imperfections, Gottschalk *et al* added an Au ad-atom to their surface, generating three possible adsorption sites: top, bridge and hollow (Figure 1.8). They concluded that all three molecules formed strong sulfur-gold bonds, but whereas the sulfur atom preferred to bind to the hollow site, there is a preference for mercapto and methyl-thiolate to adsorb on the bridge site. Based on this paper, we adopt a similar surface model in our work, where three possible chemisorption sites are created around an ad-atom: "on-top", "side-on" and "hollow" for binding of the NCS-ligands. On-top geometries bind only with the isolated ad-atom on the surface, side-on geometries interact with two atoms (the ad-atom and one on the surface), binding in a bridge site while hollow geometries bind *via* three atoms in a hollow site.



[Figure 1.8] Three possible chemisorption sites; "on-top", "side-on" and "hollow"

The variety of adsorption sites affects not only the conformational structure of the adsorbed molecules but also their electronic structure and their spin states. It is well-known that spin crossover can be a cooperative effect, and Letard *et al* have observed light-induced excited spin state trapping (LIESST) of a spin crossover compound, $Fe_xZn_{1-x}(phen)_2(NCS)_2$ with variety of concentration of zinc

atoms.[27] They concluded that the LIESST temperature is defined by interactions between the molecules and temperature. As cooperativity arises from elastic interactions between iron centres, the strength of cooperatively decreases with increasing dilution and thus increasing distance between the interacting iron centres. More important in the context of Chapter 3 is the influence of the surface on spin crossover compounds. M. Gruber *et al*. have explored the chemisorption of Fe(II)$(phen)_2(NCS)_2$ complexes on metallic surface such as Cu(100) and Au(111)[28] and showed that a strong interaction with the substrate in the form of chemisorption makes it energetically costly for the molecule to change configuration. Our aim in this final chapter is then to explore the extent to which surface adsorption alters the spin crossover behaviour of a model iron complex (Figure 1.9).



[Figure 1.9] Schematic diagram of a unit cell with a SCO molecule adsorbed in the 'on-top' geometry

2. Methodology

This thesis describes two quite distinct types of calculations. The initial stages of each section are concerned with the structure and energies of molecules that are isolated in the gas-phase (all calculations were done with the ADF software package).[29, 30] The second stage, where we are concerned with adsorption onto a periodic gold surface, requires the techniques of solid-state computational chemistry, and are performed using the VASP software package.[31, 32, 33] In this Chapter I give an introduction to the key concepts that underpin both of these methods.

2.1. Elementary concepts of quantum mechanics

The primary goal of quantum mechanics is to obtain a solution of the Schrödinger equation: the wavefunction, Ψ, contains information about the observable properties of a system. The Born interpretation of the wavefunction is that the square of the wavefunction, Ψ^2, represents a probability of finding a particular electron in a defined volume. The Hamiltonian operator, $\hat{H}$, represents the sum of the kinetic and potential energies of the system, and delivers the total energy of the system, E.

$$\hat{H}\Psi = E\Psi \qquad \textbf{(Equation 1)}$$

Wavefunctions for systems with a single electron (such as a hydrogenic atom) can often be solved exactly but extension to systems with more than one electron is considerably more complex, as it includes electron-electron interaction terms. For a system of N electrons and M nuclei described by position vectors r_i and R_A, respectively, the Hamiltonian operator can be formulated as:

$$\hat{H} = -\sum_{i=1}^{N}\frac{1}{2m_i}\nabla_i^2 - \sum_{A=1}^{M}\frac{1}{2M_A}\nabla_A^2 - \sum_{i=1}^{N}\sum_{A=1}^{M}\frac{Z_A}{r_{iA}} + \sum_{i=1}^{N}\sum_{j>i}^{N}\frac{1}{r_{ij}} + \sum_{A=1}^{M}\sum_{B>A}^{M}\frac{Z_A Z_B}{R_{AB}}$$

(Equation 2)

where r_{iA} is the distance between the ith electron and the Ath nucleus, r_{ij} is the distance between the ith and jth electrons, and the distance between Ath and Bth nuclei is R_{AB}. m_i indicates the mass of an electron. M_A and Z_A are the mass and

atomic number of nucleus A, respectively. The terms in Equation 2 above can be identified as, the operator for the kinetic energy of electrons, T_e, the kinetic energy of nuclei, T_n, the attractive Coulomb interaction between the electrons and nuclei, V_{en}, and the repulsive interactions for the electrons as well as the nuclei, V_e, V_n, respectively. Hence, the Hamiltonian operator can be cast into a more compact form as

$$\hat{\mathrm{H}} = T_e + T_n + V_{en} + V_e + V_n \qquad \textbf{(Equation 3)}$$

For many-particle systems we must resort to approximate solutions, because of the existence of the pairwise interactions between particles in the Hamiltonian; the motion of each particle is dependent on that of all the others.

The Born-Oppenheimer approximation is introduced in order to simplify the full Hamiltonian: this approximation rests on the fact that, due to their higher mass, the nuclei in a molecule move much more slowly than the electrons. Therefore, the electrons can be considered to be moving in the constant field of the nuclei, rapidly adjusting their distribution to the changing nuclear geometries. As a result, the motion of the electrons and nuclei can be considered separately. If the nuclei are held fixed, T_n can be defined as zero and V_n becomes constant. The remaining terms are collected into the electronic Hamiltonian,

$$\hat{\mathrm{H}}_e = T_e + V_e + V_{en} \qquad \textbf{(Equation 4)}$$

According to the variation theorem, the expectation value for the energy that is calculated with a trial wave function Ψ cannot be lower than the true energy of the ground state of the system, and the equality holds when Ψ is identical to the true wavefunction Ψ_0. The variation principle therefore provides a criterion for the optimization of a trial wave function: since the expectation value of the Hamiltonian is always an upper bound to the exact ground state energy, if an approximate wavefunction is used, the procedure to obtain an improved wavefunction is to vary the parameters in terms of which Ψ is expressed until the expectation value for the energy reaches its minimal value.

With these concepts, we seek an approximate solution of the electronic Schrodinger equation, a wavefunction which describes the motion of N electrons

in the potential field of M stationary nuclei point charges. When electronic coordinate and nuclear coordinates are defined as $\boldsymbol{r}$ and $\boldsymbol{R}$, the electronic Schrodinger equation with electronic wavefunction, Ψ_e, can be formulated as

$$\hat{\mathrm{H}}_e \Psi_e(\boldsymbol{r}; \boldsymbol{R}) = E_e \Psi_e(\boldsymbol{r}; \boldsymbol{R}) \qquad \textbf{(Equation 5)}$$

The energy $E(\boldsymbol{R})$ provides the potential for nuclear motion, in other word, the nuclei move on a potential energy surface obtained by solving the electronic problem. For a polyatomic system $E(\boldsymbol{R})$ will have the form of a Potential Energy Surface of dimensionality 3M, where M is the number of nuclei. Geometry optimization involves the exploration of potential energy surfaces and localization of stationary points: minima on the PES correspond to equilibrium structures while first-order saddle points correspond to transition states.

2.2. Hartree-Fock approximation

The fundamental challenge in solving the Schrödinger equation is the presence of pairwise Coulomb interactions. The underlying idea of the Hartree-Fock (HF) method is to treat those electron-electron repulsions in an average way. Each electron is considered to be moving independently in a potential which is the average due to all remaining electrons. The minimization procedure reduces the N-particle problem to a set of one-particle eigenvalue problems known as the Hartree-Fock equations

$$\hat{f}_i \Psi_i = \varepsilon_i \Psi_i \qquad \textbf{(Equation 6)}$$

An orbital Ψ_i is an eigenfunction of the effective one-particle Hamiltonian $\hat{f}_i$, known as the Fock operator, with corresponding eigenvalue, energy ε_i. The Fock operator for each electron is the sum of the core Hamiltonian operator $\hat{h}_i$ and an effective one-electron potential termed the HF potential

$$\hat{f}_i = \hat{h}_i + \hat{V}_i = -\frac{1}{2} m_i \nabla_i^2 - \sum_{A=1}^{M} \frac{Z_A}{r_{iA}} + \sum_{i=1}^{N} (\hat{J}_i + \hat{K}_i) \qquad \textbf{(Equation 7)}$$

$\hat{V}_i$ represents the potential energy term due to electron-electron repulsion, where $\hat{J}_i$ is the Coulomb operator and $\hat{K}_i$ is the exchange operator. The Coulomb operator accounts for the classical Coulomb repulsion between electrons, while the exchange operator represents a modification of this energy that can be ascribed to the effects of spin correlation. Each orbital Ψ_i is obtained as a solution to the eigenvalue equation with the corresponding operator $\hat{f}_i$. Since $\hat{f}_i$ depends on the form of the orbitals describing all other electrons, an iterative approach is required in order to solve the HF equation. This procedure is known as the Self-Consistent Field (SCF) method: by initially guessing a set of orbitals, the average potential can be calculated and, using this value for the field, a new set of orbitals is obtained by solving the HF equations and the cycle is repeated until self-consistency is reached. In practice, the orbitals Ψ_i are converted to a set of matrix equations by a finite set of basis functions. Each molecular orbital is expanded in terms of these basis functions, which are commonly referred to as atomic orbitals.

2.3. Density Functional Theory

The development of density functional theory (DFT) has introduced a different methodological philosophy from Hartree-Fock theory. DFT begins with the concept of electron density as the central variable instead of the conventional wavefunction, which brings significant advantages. The electron density depends on fewer variables than the wavefunction: a wavefunction for a N-electron system depends on a total 4N coordinates (three spatial and one spin variable for each of the N electrons). The complexity of such an object increases rapidly with the number of electrons in the system. In contrast, electron density is an object in three-dimensional space, and therefore only depends on three spatial coordinates, irrespective of the number of electrons in the system.

Central to DFT is the idea that the energy of an electronic system can be expressed in terms of the electron density $\rho(\boldsymbol{r})$. The electronic energy is said to be a functional of the electron density and denoted $E(\rho)$, in the sense that for a given function $\rho(\boldsymbol{r})$ there is a single corresponding energy. We can write the energy decomposition in terms of the components, each of which depends on the density as

$$E(\rho) = V_{en}(\rho) + T(\rho) + V_{ee}(\rho) \qquad \textbf{(Equation 8)}$$

$V_{en}(\rho)$ describes potential energy of nuclei-electron attraction. $T(\rho)$ and $V_{ee}(\rho)$ represent kinetic energy and electron-electron repulsion respectively. $T(\rho)$ and $V_{ee}(\rho)$ are universal, which means that their form is independent of the particular system. On the other hand, $V_{en}(\rho)$ is a system-dependent value.

The electron-electron repulsion term, $V_{ee}(\rho)$, can then be decomposed into a classical Coulomb component (the classical electrostatic repulsion experienced by an electron gas) and a separate *exchange-correlation term*, which attempts to capture the effects of spin correlation defined by K in the Hartree-Fock approach and also the correlation between paired electrons which is intrinsically beyond the Hartree-Fock approach. If the exact form of the exchange-correlation functional were known, DFT would be exact. As it is not, the main goal of DFT developmental research is to find better exchange-correlation functionals. A useful way of thinking about the exchange-correlation potential in terms of

electron density involves so-called exchange-correlation holes. Considering that the first electron is at coordinate r_1, then the exchange-correlation hole is defined as the difference between the probability of finding the second electron at r_2, where the electron is treated as a classical particle. The exchange-correlation hole can then be divided into two components: a Fermi hole, which accounts for the reduced probability of finding an electron with the same spin near the reference electron; and a Coulomb hole, which is due to the electrostatic interaction of electrons of either spin.

2.4. The local density approximation (LDA)

The precise form of the exchange-correlation energy in molecules is unknown, but an analytical solution is available for a hypothetical uniform electron gas: Slater showed that the energy is related to the density at a specific point, the so-called Local Density Approximation (LDA). Physically the uniform electron gas represents a model of an idealised metal consisting of completely delocalised valence electrons moving in a uniform positive background charge. This is a reasonable model for simple metals such as sodium. But, in atoms and molecules, the electron density is usually anything but homogenous and the model is a significant over-simplification. The advantage of LDA is that the exchange and correlation energies are known to a very high degree of accuracy. Extending the LDA to the unrestricted case, where spin-up and spin-down orbitals can be different, gives the local spin-density approximation (LSDA). In general, those approximations provide accurate geometries, harmonic frequencies and charge moments. However, there is a larger error in energies, as it typically over binds. The success of the LDA is attributable to the exchange-correlation hole in molecules, which have a more homogeneous electron distribution than atoms. However, the LDA will have the highest degree of accuracy where there are only small distances between the reference electron and the electron of interest. With variation in charge density, the accuracy decreases as the distance between the reference electron and another increases.

2.5. The generalised gradient approximation (GGA)

To improve the description of the Fermi and correlation hole, a logical step is to let the energy depend not only on the density, but also the gradient of the density. Hence, LDA is the first term of the expansion, and a better approximation would extend the series to higher terms. The exchange-correlation hole is decomposed into its exchange and correlation components, and approximations for each term are sought individually. There have been several suggestions of how to apply these, including semi-empirical functionals which contain parameters that are calibrated against reference values, rather than being derived from first principles. For example, one of the most popular expressions for the exchange hole was developed by Becke, and contains an empirical parameter determined

by a least-squares fit to the exactly known exchange energies of the noble gases, He-Rn. One of the most widely used expressions for the correlation hole is Perdew's, which is fitted to the correlation energy of the neon atom.

2.6. Hybrid functionals

The contribution of exchange to the overall exchange-correlation hole is much more significant than that from correlation, and the approximations in the LDA and GGA approximations have undesirable effects: electrons are typically too strongly bound. In Hartree-Fock theory, in contrast, the exchange energy of Slater determinant is determined exactly, and electrons are typically bound to the weakly. As a result, a mixture of Hartree-Fock and DFT exchange seems a reasonable compromise, and this is found in so-called hybrid functionals. The exact combinations are determined by fitting to experimental data. Hybrid functionals such as PBE0 and s12H have proved particularly useful in accurate determination of spin states.

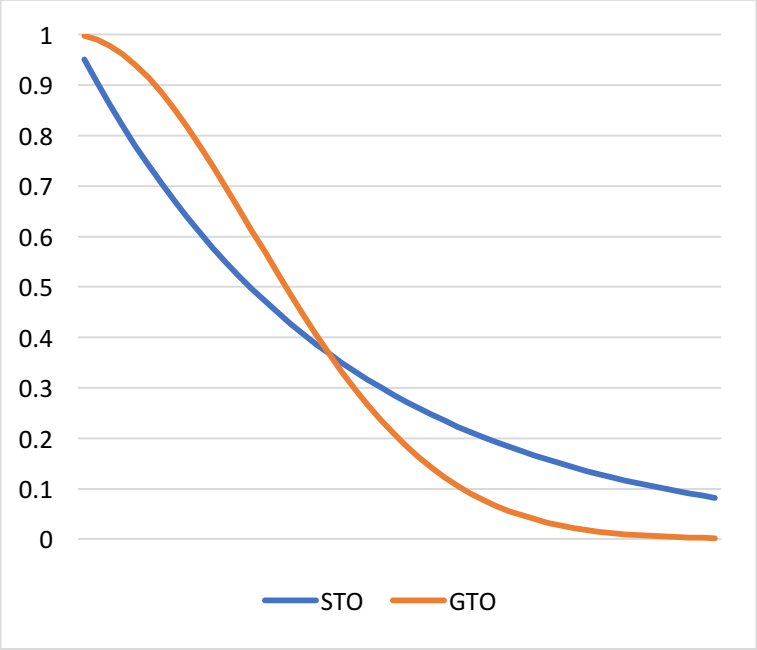
2.7. The Kohn-Sham approach to DFT

One of the major steps in the development of DFT as a useful tool came from the Kohn-Sham approach. Although it is known from the Hohenberg-Kohn theorems that the kinetic energy is uniquely defined by the density, practical ways to compute it from an arbitrary density have proved very difficult to identify. Kohn and Sham decomposed the kinetic energy into two parts, one for a system of non-interacting electrons with precisely the same density as the real system, for which kinetic energy can be calculated exactly; and secondly a small correction term, which is incorportated into the exchange-correlation term.

2.8. Localised basis sets

A basis set contains a number of predefined basis functions which are brought together in a specific linear combination to describe a molecular orbital. These basis functions can be classified into two main categories, specifically Slater-type orbitals (STO) and Gaussian-type orbitals (GTO). Although Slater type orbitals produce optimal atomic orbitals, they are not as mathematically convenient to use. Gaussian-types orbitals are the usual alternative functions to the STO because the integration of products of GTO is much more facile than products of STO. The key property is that the product of two GTOs centered on different atoms reduces to a single Gaussian at a shifted center. In practical terms, this means that computational codes that rely on Hartree-Fock theory as a starting point (Gaussian, Molcas, for example) are based almost exclusively on GTOs. However, GTOs have drawbacks: they lack the proper cusp behavior of the STOs and also reduce in amplitude too rapidly at large distance. To address this problem, we can approximate the shape of an STO by taking a linear combination of several primitive GTOs with different coefficients and their respective exponents. The accuracy and degree of complexity of a basis set are dependent on the number of contracted functions employed to represent each atomic orbital. A minimal basis set contains a single STO per occupied orbital. A well-known example of a minimal basis set is STO-3G, which has three primitive GTOs that combine to represent an STO. This type of basis set is known as single-*zeta* basis set. More sophisticated basis sets can be built by adding two or more basis functions for each atomic orbital, which give rise to double *zeta*, triple *zeta* and

quadruple *zeta* basis sets. The valence electrons are most important for the formation of bonds, so it is important to include a more accurate description of the valence electrons. In codes that have evolved specifically to deal with density functional theory, however, the rapid computation of 2-electron integrals is not required because the key variable is the total density, not the wavefunctions of the individual electrons. Therefore the key advantage of using GTOs is lost, and the more physically accurate STOs are used instead. This is the case in the ADF software package used in this thesis.



[Figure 2.1] Distribution graph of STO and CTO

2.9. Amsterdam Density Functional (ADF) software

All of the computational work on single metal complexes is implemented by Amsterdam Density Functional (ADF). In the first chapter on Cu/Ag/Au complexes, all calculations are performed with the PBE functional and a TZP basis set. For the chapter dealing with spin crossover, we have considered a wider range of functionals (PBE, OPBE, B3LYP, B3LYP*, PBE0, s12h), and applied a TZP basis set on the metal with DZP on the surrounding atoms.

2.10. Cluster and Periodic ab-initio calculations

The calculations described above can be considered as 0-dimensional, and such techniques can be applied to nanoparticles, molecules and nanostructures. For a long time this type of cluster approach was applied to increasingly large surface models using codes such as Gaussian, ADF and others. Accurate simulation of crystalline bulk materials, however, requires a periodic approach as implemented in VASP, CASTEP, etc. The use of periodic boundary conditions combined with a vacuum slab separating surface layers in two neighboring unit cells allows surface phenomena to be studied as a quasi two-dimensional approach. This periodic problem, however, requires a rather different computational framework, particularly with regard to basis functions because the highly localized GTOs described above are not well suited to problems of this type.

2.11. Plane wave and LCAO basis sets

In the previous section I described localized basis sets of the GTO and STO kind, Crystals are necessarily periodic and plane waves describe this situation well as they propagate through the crystal. One should note that both methods should converge to the same result in the limit of an infinite basis, and the choice of the basis function is important primarily from the perspective of computational cost. For solid-state systems, plane wave basis sets better reflect the inherent periodicity of the system. In a plane wave basis set, valence electrons are modelled in terms of sine and cosine functions. In periodic systems, orbitals are expanded to a set of plane waves as

$$\Psi(\boldsymbol{r}) = \boldsymbol{A}e^{\boldsymbol{ikr}} + \boldsymbol{B}e^{-\boldsymbol{ikr}} \qquad \textbf{(Equation 9)}$$

where **k** is the wave vector, the value corresponding loosely to the size of the basis. The plane-wave cut-off value therefore defines the basis size by specifying the highest energy, and therefore the highest wave-vector, to be used. A large cut-off therefore describes orbitals more accurately, but at greater computational expense.

2.12. Brillouin zone sampling

The Brillouin zone (BZ) is a uniquely defined primitive cell in reciprocal space. The Wigner-Seitz cell is defined by the planes that are the perpendicular bisectors of the vectors from the origin to the reciprocal lattice points. The energies of particular orbitals can vary substantially throughout the Brillouin zone, and therefore an accurate calculation of energy requires statistical sampling of the energy at appropriate points in the BZ. In the VASP software, the BZ is sampled on a (k_x, k_y, k_z) grid, and an exact energy is obtained, in principle, by sampling on an infinitely fine grid. In practice, the number of points on the grid is increased systematically until the number of interest converges, at least so far as this is compatible with available resource.

2.13. Pseudopotential

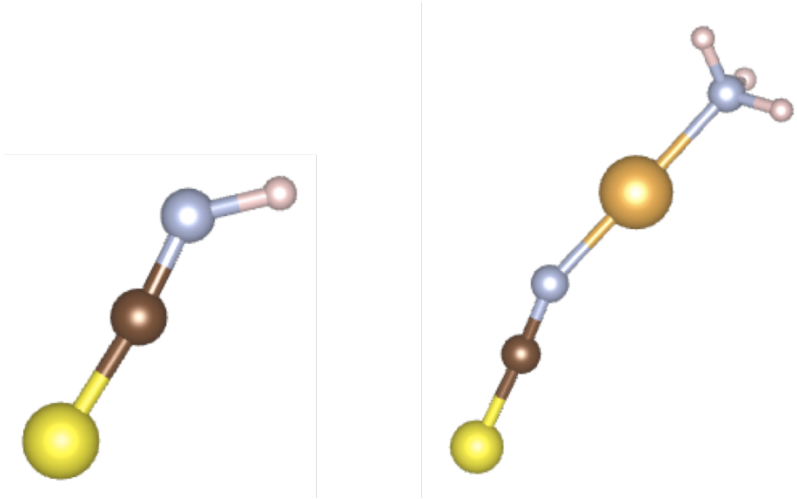
The description of the inner regions of orbitals with high principal quantum number, where curvature is high, is extremely problematic with a plane-wave basis as very high cutoffs are required to model this curvature. As a result, so-called pseudopotentials are used to describe the influence of these inner core electrons on the outer valence region. The primary application in electronic structure is to replace the strong Coulomb potential of the nucleus and the effects of the tightly bound core electrons by an effective ionic potential acting on the valence electrons. A pseudopotential can be generated in an atomic calculation and then used to compute properties of valence electrons in molecules or solids since the core states remain almost unchanged.

All surface calculations are done using the Vienna Ab-initio Software Package (VASP). The gold surface is described by either 3 x 3 or 6 x 6 slabs with a vacuum layer. The density functional is PBE, with a typical plane-wave cut-off of 450 and a 5 x 5 sampling of the BZ in two dimensions. These choices are explicitly tested

for convergence at the start of chapter 4. One further aspect of the solid-state calculations is the use of the so-called "Hubbard-*U*" parameter to mimic the effects of strong correlation. A finite value of U introduces a penalty for double occupation of any level, and so favours unpaired spins. In this sense, it typically replicates the effects of adding Hartree-Fock exchange in hybrid functionals used in gas-phase calculations.

3. Structure and property of L-M-NCS complexes (M = H^+, Au^+, Ag^+, Cu^+) with ligands (L = NH_3, CN^-)

3.1. Introduction

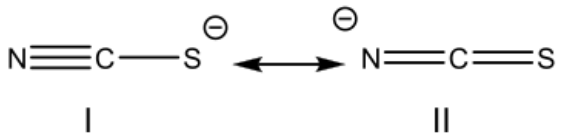


[Figure 3.1] H-NCS (left) complex, H_3N-Au-NCS (right)

In the first section of the results, I will discuss in detail the electronic structure of the NCS^- anion, in combination with a range of counter-ions. These ions increase in complexity from a simple proton (H-NCS, Figure 3.1, left) through isolated metal cations of group 11 (Cu^+, Ag^+, Au^+) through to more complicated ligated species such as Cu-L, L = NH_3, CN^- (Figure 3.1, right). The d^{10} transition metal in the group 11 presents variable coordination numbers and ML_2 linear complexes occur in catalytic reaction mechanisms.[34] For example, Cu^+ reacts with PH_3, forming the *di*- and *tri*- coordinated complexes while Ag^+ and Au^+ form linear-coordinated complexes. In addition, in the gas phase, mono-coordination complexes can be also found.[35]

The purpose here is to establish the extent to which coordination at one end of the NCS^- unit (typically nitrogen) influences the bonding within the *tri*-atomic unit and, ultimately, the ability of the remote atom to bind to a metal surface. As anticipated in the introduction, the discussion will be based on the limiting resonance structures of the NCS^- anion (Scheme 3.1 below) where the multiplicity of the N-C and C-S bonds varies which can influence the electron transport properties and the stochastic fluctuations in STM.

Any particular case represents some intermediate point between these two limits of resonance forms. The two forms differ most obviously in the position of the formal negative charge, and so Mulliken charges provide some guidance to the nature of the dominant resonance form. Mulliken charges are, however, notoriously dependent on computational details, notably the basis set. The definition of atomic charge in molecules remains quite arbitrary and the use of other partition schemes often leads to quite different net atomic charges,[36] making them difficult to compare for different compounds. Changes in bond length offer a different perspective, but again differences are often small. Bond angles are a third, and rather more sensitive, indicator because in resonance structure I below the triple N-C bond leaves only one lone pair available on nitrogen (sp hybridization). The rules of VSEPR then suggest linear coordination (*i.e.* an M-N-C angle of 180˚). In resonance structure II (Scheme 3.1), in contrast, the nitrogen is sp^2 hybridized and the presence of a second lone pair at the nitrogen dictates an angle of 120˚. Thus, the precise angle adopted is a sensitive measure of the hybridization state of the nitrogen.



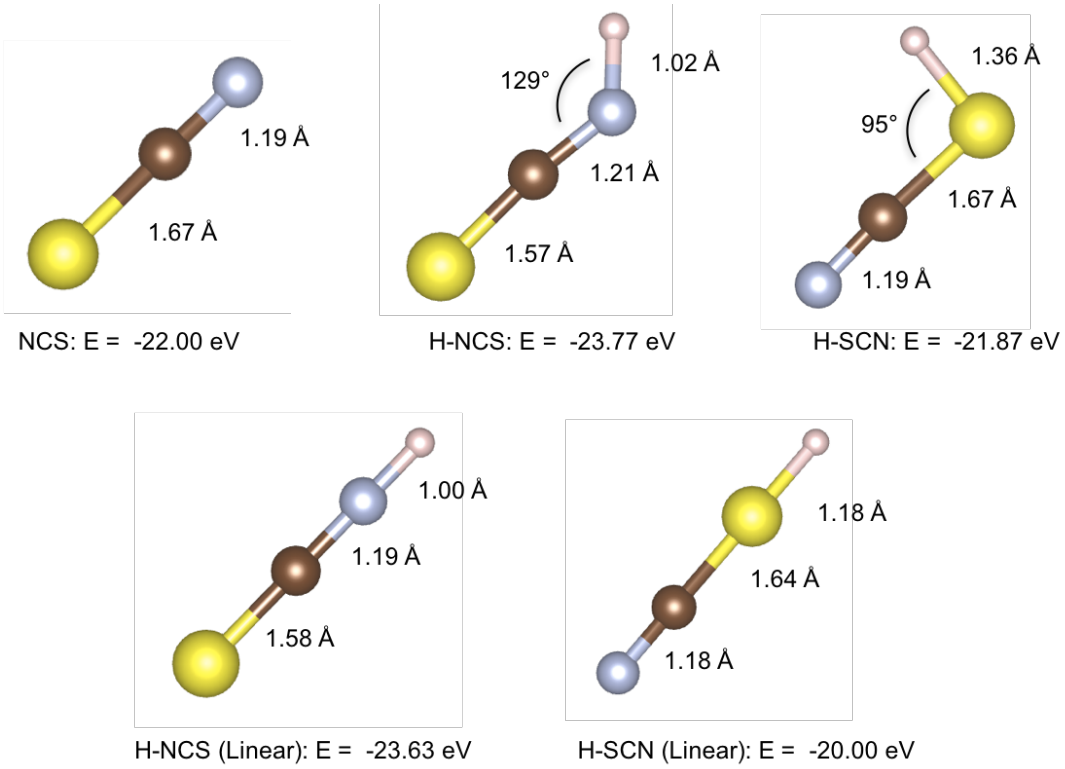
[Scheme 3.1] Two resonance forms of NCS^- ligands

3.2. H-NCS and its conjugate base, NCS^-

Thio-cyanic acid is a key molecule for electron transport and STM studies due to the tendency to bind to an Au surface, and its ability to bind to a metal centre. The various isomers of thio-cyanic acid have been studied previously.[37] Thomas Custer *et al*. explored the entire potential energy surface in the gas phase.[38] The motivation for this work was the possibility that H-NCS may be present in the interstellar medium. The authors' survey identified key minima (H-NCS, H-SCN) on the potential energy surface, shown in Figure 3.2 below, and we have located the same structures using our chosen DFT protocol (PBE, TZP). The relative energies and structural parameters from our DFT study are very similar to those reported recently. Of those isomers, the two most stable contain an N-C-S unit, protonated either at the nitrogen or at the sulfur. The N-protonated isomer, H-NCS, is more stable than the alternative NCS-H by 1.90 eV. In the following discussion, we focus only on the two most stable structures.

The N-H, N-C and C-S bond lengths of 1.02 Å, 1.21 Å and 1.57 Å in the equilibrium H-NCS isomer are typical of single, double and double bonds, respectively, and the large positive charge on the proton (Q(H) = +0.42) is consistent with the acidic nature of the molecule. The optimised bond angle of 129˚ is, as noted above, indicative of sp^2 hybridisation. In an experimental study, a similar angle is observed with a self-assembled monolayer on an Au surface. In subsequent sections, we will consider this angle in detail, so it is useful to examine the energetic significance of the bending. A further calculation where perfect linearity is imposed on the H-NCS unit (*i.e*. all angles are 180˚) is also shown in Figure 3.1 (linear), where the stabilisation due to bending is only 0.14 eV. The bending mode is therefore very soft, even over a wide range, and so we must be careful in attaching too much significance to this angle when considering optimised structures. In the linear geometry, the N-H bond becomes marginally shorter (1.00 Å vs 1.02 Å), as does the N-C bond (1.19 Å vs 1.21 Å) while the C-S bond lengthens by 0.01 Å. These relatively minor changes in bond length are accompanied by a larger change in Mulliken charges, with the proton becoming substantially more positive (Q(H) = 0.62 vs 0.42), Q(N) less negative and Q(S)

more negative. All of these indicators are consistent with a small shift from resonance structure II to resonance structure I in the linear isomer.



[Figure 3.2] Optimised structure and energy of NCS^- molecule and H-NCS, H-SCN isomers

	NCS^-	H-NCS	H-NCS (Linear)	H-SCN	H-SCN (Linear)
D(N-C)/D(C-S)	0.71	0.77	0.75	0.71	0.72
Q(H)	–	0.42	0.62	0.07	0.25
Q(N)	-0.64	-0.36	-0.27	0.12	-0.44
Q(S)	-0.48	-0.05	-0.10	0.27	0.25
Q(N)/Q(S)	1.34	7.66	2.70	0.42	-1.73

[Table 3.1] D(N-C)/D(C-S) ratio and Mulliken charges for NCS^-, H-NCS and H-SCN (D: bond distance, Q: Mulliken charge)

Turning to the less stable NCS-H isomer, the optimised bond lengths (N-C = 1.36 Å, C-S = 1.68 Å and S-H = 1.43 Å) are typical of triple, single and single bonds, respectively, consistent with a dominant contribution from resonance structure I. The H-S-C bond angle is very acute (H-S-C = 95°), typical of heavier elements

where bond angles close to 90˚ maximise the contributions of the p orbitals to the bonding. Thus, imposing a linear geometry in this case is more energetically costly (ΔE = 1.87 eV). The conformational parameters are, however, only affected to a very minor extent as resonance structure I dominates in both linear and bent forms. Finally, turning to the conjugate base, we can immediately identify structural characteristics that are more typical of resonance structure form I, most notably the long C-S bond which is similar to that in NCS-H. The negative charge on sulfur is also extremely high in NCS^-, much higher than in H-NCS.

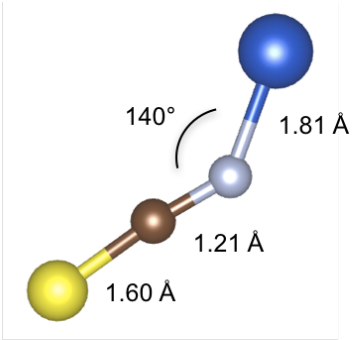
In the following sections, we explore the corresponding potential energy surfaces for the cations of the group 11 transition metals, Cu^+, Ag^+ and Au^+ with the aim of establishing (a) how the balance between N- and S- coordination is affected and (b) how the balance between resonance structures, as measured by charges, bond lengths and bond angles, changes.

3.3. M-NCS, M = Cu^+, Ag^+ and Au^+

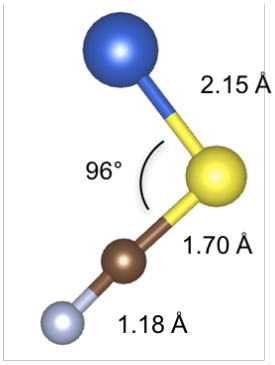
The corresponding stationary points for M-NCS, M = Cu^+, Ag^+, Au^+ are collected in Figure 3.3-3.5. We note immediately that whilst the order of the N- and S-coordinated isomers is the same as for the thio-cyanic acid for the Cu^+ complex, albeit with a smaller energetic separation (vs 0.07 eV), the order is reversed for both Ag^+ and Au^+, with sulfur coordination preferred by 0.07 eV (Ag) and 0.29 eV (Au). This reversal is typical of the classically 'soft' nature of Au^+ and, to a lesser extent Ag^+, both of which generally form more stable bond to soft donor atoms such as S and P.

The structural parameters and Mulliken charges are shown in Table 3.2-3.4 for the nitrogen-bound isomers of M^+ (M = Cu^+, Ag^+ Au^+), and there are many similarities compared to the corresponding isomer of thio-cyanic acid itself. The M-N-C angle varies between 125° and 140° (cf. 129° for H-NCS), indicating dominant sp^2 hybridisation (resonance structure II), and the Mulliken charges also indicate a substantial negative charge localised on N. The C-S bond length is, however, distinctly longer in all three complexes than in H-NCS (1.60-1.61 Å vs 1.57 Å) and Q(S) somewhat more negative, suggesting that the balance has shifted somewhat towards resonance structure I. The energetic driving force for bending increases in the sequence Cu < Ag < Au, with the linear isomer for the latter lying 0.35 eV higher in energy.

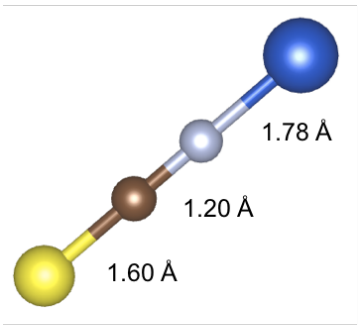
For the S-coordinated isomers, we can also note similar patterns to those in NCS-H. The optimised bond lengths (N-C = 1.18 Å, S-C = 1.70 Å) are typical of triple and single bonds as the predominant contribution of resonance structure I in Cu^+, Ag^+ and Au^+. In terms of M-S-C bond angles, all are close to the 90° (M-S-C = 94°-101°), maximizing the overlapping in p orbitals. Given the acute angles, linearization costs a significant amount of energy (Cu = 1.50 eV, Ag = 1.23 eV, Au = 1.49 eV). Mulliken charge analysis suggests that, although the contribution of resonance form II increases, Q(S) does not change dramatically.



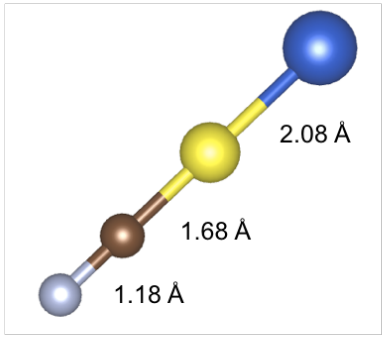
Cu-NCS: E = -21.72 eV



Cu-SCN: E = -21.65 eV



Cu-NCS (Linear): E = -21.65 eV

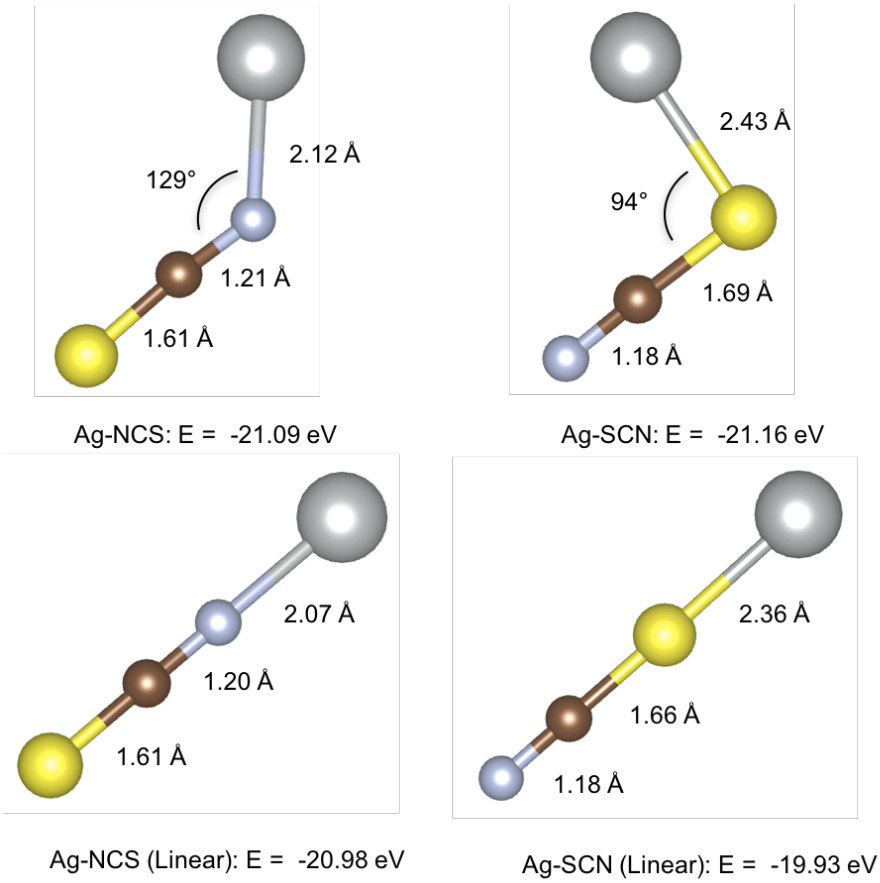


Cu-SCN (Linear): E = -20.15 eV

[Figure 3.3] Optimised structure and energy of Cu-NCS and Cu-SCN isomers

	Cu-NCS	Cu-NCS (Linear)	Cu-SCN	Cu-SCN (Linear)
D(N-C)/D(C-S)	0.75	0.75	0.69	0.71
Q(M)	0.50	0.58	0.31	0.40
Q(N)	-0.42	-0.36	-0.27	-0.28
Q(S)	-0.12	-0.16	-0.05	-0.10
Q(N)/Q(S)	3.50	2.26	5.47	2.74

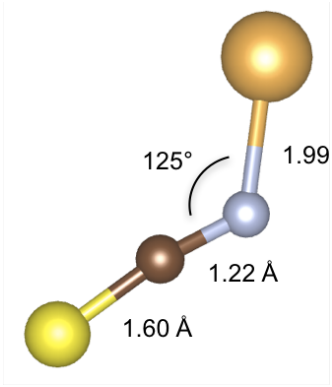
[Table 3.2] D(N-C)/D(C-S) ratio and Mulliken charges for Cu-NCS and Cu-SCN (D: bond distance, Q: Mulliken charge)



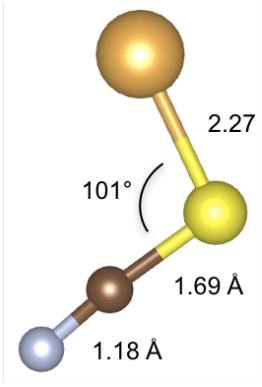
[Figure 3.4] Optimised structure and energy of Ag-NCS and Ag-SCN isomers

	Ag-NCS	Ag-NCS (Linear)	Ag-SCN	Ag-SCN (Linear)
D(N-C)/D(C-S)	0.75	0.74	0.70	0.71
Q(M)	0.60	0.71	0.45	0.57
Q(N)	-0.48	-0.44	-0.29	-0.30
Q(S)	-0.15	-0.20	-0.15	-0.26
Q(N)/Q(S)	3.18	2.18	1.89	1.17

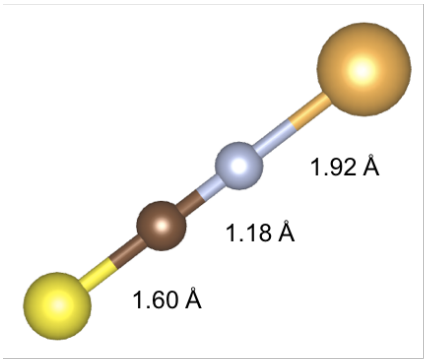
[Table 3.3] D(N-C)/D(C-S) ratio and Mulliken charges for Ag-NCS and Ag-SCN (D: bond distance, Q: Mulliken charge)



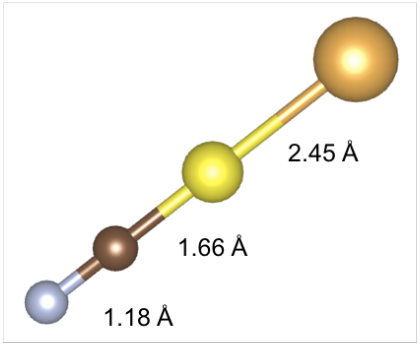
Au-NCS: E = -20.88 eV



Au-SCN: E = -21.17 eV



Au-NCS (Linear): E = -20.53 eV



Au-SCN (Linear): E = -19.68 eV

[Figure 3.5] Optimised structure and energy of Au-NCS and Au-SCN isomers

	Au-NCS	Au-NCS (Linear)	Au-SCN	Au-SCN (Linear)
D(N-C)/D(C-S)	0.76	0.75	0.69	0.71
Q(M)	0.42	0.62	0.25	0.60
Q(N)	-0.46	-0.42	-0.25	-0.30
Q(S)	-0.05	-0.14	-0.03	0.60
Q(N)/Q(S)	9.10	2.90	7.90	-0.51

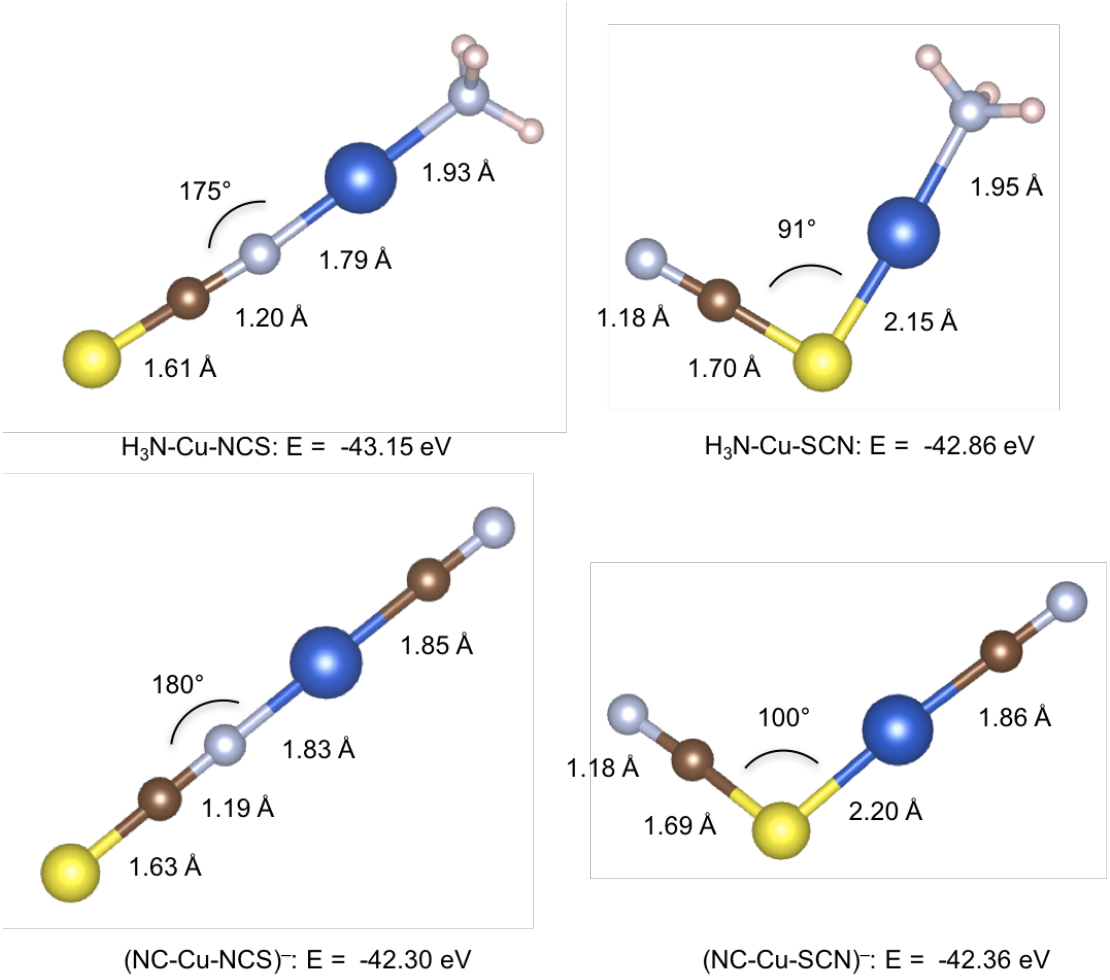
[Table 3.4] D(N-C)/D(C-S) ratio and Mulliken charges for Au-NCS and Au-SCN (D: bond distance, Q: Mulliken charge)

3.4. Potential energy surface of L-M-NCS (L = NH_3 and CN^-), M = Cu^+, Ag^+ and Au^+

Having established the influence of coordinated metal ions, Cu^+, Ag^+ and Au^+, on the geometry of a bound NCS ligand, we now consider the influence of a ligand bound *trans* to the NCS unit. Specifically, we consider a weak σ-donor, NH_3, and a rather stronger σ-donor, CN^-. The structures of the NH_3 and CN^- ligated complexes are shown in Figures 3.6-3.8 and the Mulliken charges are summarized in Tables 3.5-3.7, which should be compared to the corresponding data for the ligand-free system in Figures 3.3-3.5 and Tables 3.2-3.4.

Comparing Figures 3.6 and 3.3 we note first that the N-coordinated isomer is now more stable than the alternative S-bound isomer, NCS-Cu, by 0.29 eV compared to only 0.07 eV in the ligand-free complex. The presence of a *trans* ligand therefore appears to favor binding on the nitrogen. In the strength of Cu-N bond, NCS-ligand binds stronger than NH_3 ligand as those bond distances are 1.79 Å and 1.93 Å. The N-C and C-S bond lengths are shortened and elongated by 0.01-0.02 Å, respectively, suggesting a shift towards resonance structure I. The M-N-C angle is also closer to linear in the presence of an NH_3 ligand, also consistent with a shift towards resonance structure I. The binding of NH_3 has less of an impact on the structure of the S-bound isomer due to the rather stronger Cu-S binding.

When the NH_3 ligand is replaced with CN^-, the trends observed above are further exaggerated. The NC-M-NCS angle is now perfectly linear and the Cu-NCS bond elongated to 1.83 Å, consistent with the *trans* influence of the CN^- ligand, and the C-S bond length is elongated to 1.63 Å. In this case, however, the S-bound isomer Cu-SCN becomes marginally more stable than the N-bound alternative (ΔE = -0.06 eV), indicating that the weakening of the Cu-NCS bond by the strongly donating CN^- is more significant than the weakening of the Cu-SCN bond.



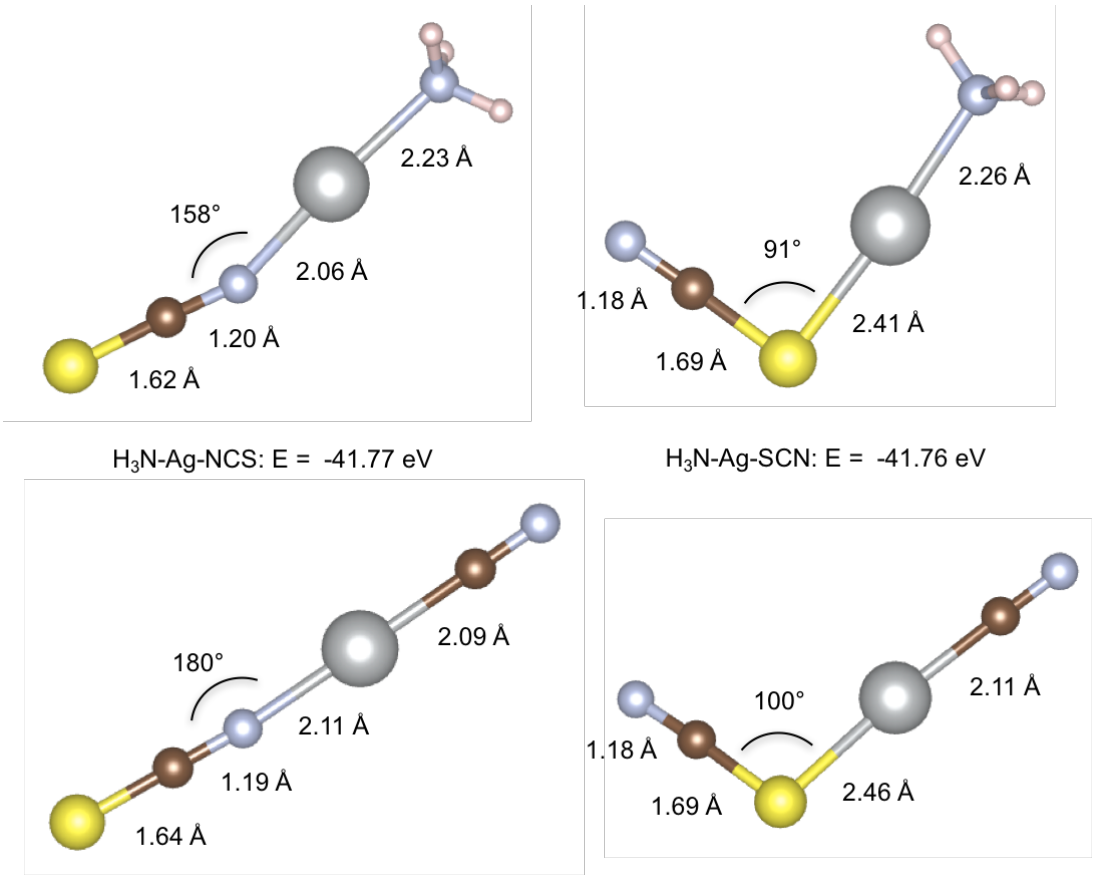
[Figure 3.6] Optimised structure and energy of L-Cu-NCS and L-Cu-SCN isomers (L = NH_3 and CN^-)

	H_3N-Cu-NCS	H_3N-Cu-SCN	(NC-Cu-NCS)$^-$	(NC-Cu-SCN)$^-$
D(N-C)/D(C-S)	0.74	0.69	0.73	0.70
Q(M)	0.43	0.25	0.21	0.11
Q(N)	-0.32	-0.31	-0.25	-0.35
Q(S)	-0.21	-0.12	-0.10	-0.22
Q(N)/Q(S)	1.56	2.56	2.43	1.62

[Table 3.5] D(N-C)/D(C-S) ratio and Mulliken charges for L-Cu-NCS (L = NH_3 and CN^-)

The corresponding data for Ag and Au are collected in Figure 3.7-3.8 and Table 3.6-3.7. The patterns identified for Cu^+ are again apparent in the data for the heavier elements. Binding NH_3 and then CN^- *trans* to the M-NCS unit gives a

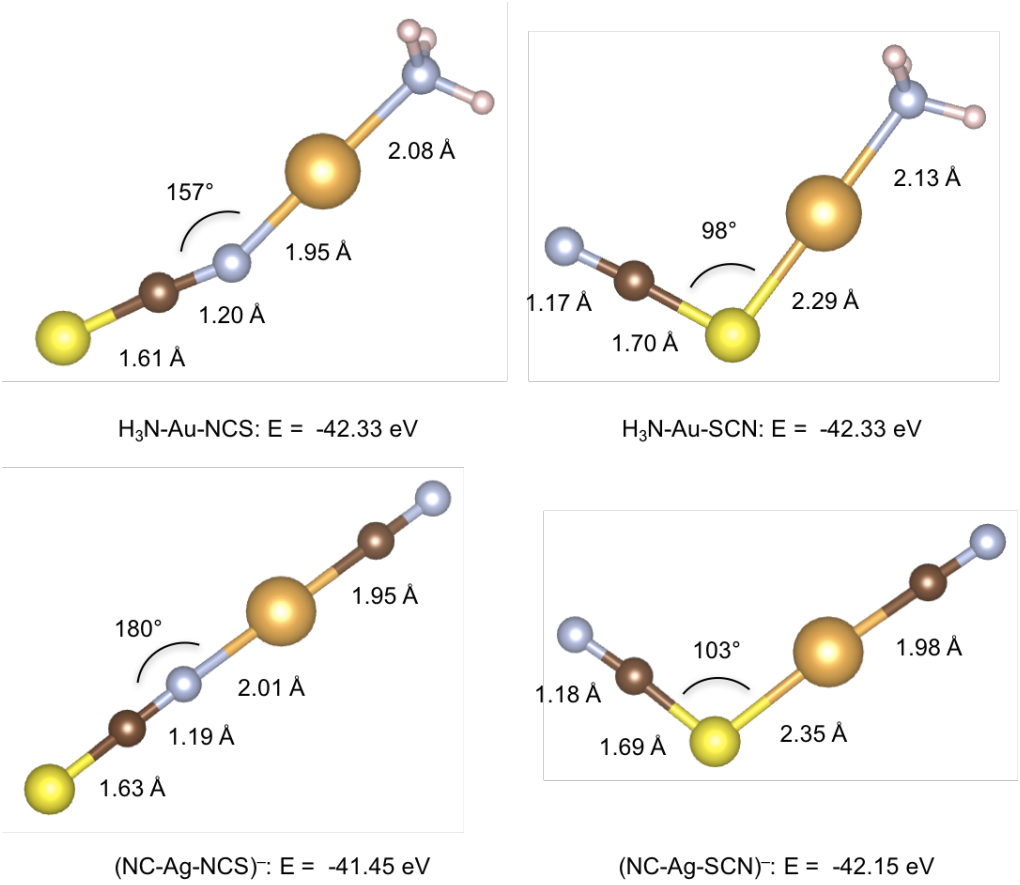
systematic preference for the -SCN over the -NCS isomer, the two being almost iso-energetic for H_3N-Ag-NCS and the S-bound isomer being preferred for NC-Ag-SCN. The C-S bond is again elongated in the CN^- complexes, and the M-N-C angle of 180˚ is indicative of sp hybridization and hence of a shift towards resonance structure I. In summary, the presence of a second ligand bound, either NH_3 or the stronger σ-donor CN^-, *trans* to the NCS unit causes subtle but non-negligible changes in the electronic structure of the NCS unit. The strong σ-donor NC-ligand, in particular, favors a linear geometry with an elongated C-S bond, consistent with a shift towards resonance structure I in Scheme 3.1.



[Figure 3.7] Optimised structure and energy of L-Ag-NCS and L-Ag-SCN isomers (L = NH_3 and CN^-)

	H_3N-Ag-NCS	H_3N-Ag-SCN	$(NC\text{-}Ag\text{-}NCS)^-$	$(NC\text{-}Ag\text{-}SCN)^-$
D(N-C)/D(C-S)	0.74	0.69	0.73	0.70
Q(M)	0.59	0.42	0.36	0.25
Q(N)	-0.43	-0.31	-0.33	-0.36
Q(S)	-0.23	-0.20	-0.35	-0.29
Q(N)/Q(S)	1.89	1.54	0.95	1.22

[Table 3.6] D(N-C)/D(C-S) ratio and Mulliken charges for L-Ag-NCS (L = NH_3 and CN^-)



[Figure 3.8] Optimised structure and energy of L-Au-NCS and L-Au-SCN isomers (L = NH_3 and CN^-)

	H_3N-Au-NCS	H_3N-Au-SCN	$(NC\text{-}Au\text{-}NCS)^-$	$(NC\text{-}Au\text{-}SCN)^-$
D(N-C)/D(C-S)	0.74	0.69	0.73	0.70
Q(M)	0.53	0.30	0.38	0.20
Q(N)	-0.43	-0.29	-0.35	-0.35
Q(S)	-0.21	-0.16	-0.34	-0.25
Q(N)/Q(S)	2.11	1.88	1.04	1.39

[Table 3.7] D(N-C)/D(C-S) ratio and Mulliken charges for L-Au-NCS (L = NH_3 and CN^-)

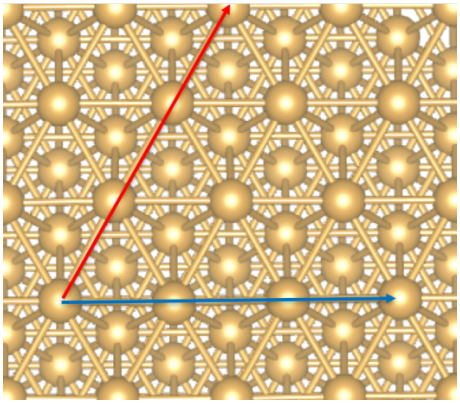
3.5. Summary

A variety of L-M-NCS and L-M-SCN complexes has been examined to probe the contribution of the two resonance forms in Scheme 3.1. In summary, H- and Cu-NCS complexes are more stable structures than their -SCN counter parts, but the opposite order is observed for Au- and Ag-NCS complexes. This highlights the affinity of the sulfur atom to a soft metal, such as an Au substrate. In terms of the shift of the resonance structure between form I and II, the C-S bond length changes from 1.57 Å in H-NCS to 1.60-61 Å in M-NCS. Moreover, the *trans* effect from NH_3 and CN^-, especially the CN^- ligand, increases the contribution of form I with C-S bond length ending 1.63-64 Å. Thus, coordination shifts the dominant NCS resonance structure to form I, which is the sulfur negative form, while M-N bond on NCS weakens. The M-N-C bending mode is very soft as change from bent to linear is 0.1-0.4 eV in H- and M-NCS complexes. In the following section, the optimised complexes introduced above are attached on an Au(111) surface and we consider what implications these changes have for binding of the molecule to a gold surface *via* the sulfur terminal of the NCS ligand.

4. Bonding of NCS complexes to a gold (111) surface

4.1 Introduction

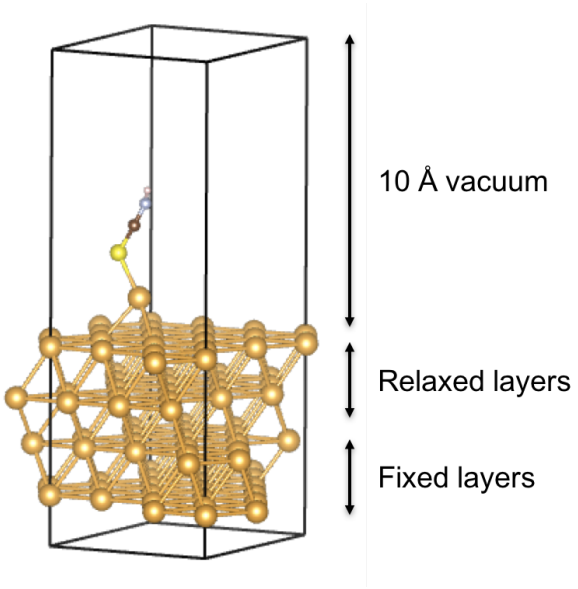
Following on from the previous chapter where we described the bonding of L-M-NCS species to isolated metal ions, we now consider the more complex problem of binding to a gold surface. This relates more directly to the experimental measurements of conductance, where the molecule is contacted by two bulk gold electrodes. The precise geometry of the junction between molecule and gold has been debated,[39] but it is unlikely to be a perfect section of an Au(111) surface – more likely is that imperfections on the surface will offer high-energy binding sites and serve as a locus for bonding. Greet Brocks *et al.*[26] have shown that the formation of self-assembled monolayers of alkane thiolate can induce significant reconstruction of the Au(111) surface, and it is conceivable that the NCS-containing species under consideration here may induce similar effects. In order to allow for this possibility, we have added an additional gold atom to the surface. We consider three possible chemisorption sites: the "on-top" site where a single molecule chemisorbs on the ad-atom, the "side-on" site where a single molecule bridges between the ad-atom and one of the atoms on the surface and the "hollow" site where it bonds in a triangular site on the Au(111) surface (Figure 2.1), which is inspired by the J. Gottschalck and B. Hammer study.[25]



[Figure 4.1] Au (111) plane with 3x3 unit cell is described in blue and red vectors

The set-up of the unit cell is shown in Figure 4.2. The Au surface is modelled by 4 layers of gold atoms, with a vacuum gap of 10 Å along the vertical axis, as done in

the Gronbeck group.[20] This distance serves to effectively isolate the slabs from each other: tests show that further increasing this distance results in very small changes to energy and geometry. In order to accommodate the presence of an ad-atom and the different possible binding sites, the unit cell is a 3 x 3 extension of the normal hexagonal unit cell in the a and b directions with a 10 Å vacuum slab. A single gold ad-atom is placed in one hollow site for the modelling of a reconstructed Au(111) surface. Three distinct binding geometries in Figure 1.9 are examined for chemisorption sites in the unit cell. In the geometry optimisations, only the top 2 layers of gold atoms are allowed to relax: the lower 2 layers were constrained to their bulk geometry. All of the calculation is done using density functional theory with a GGA functional (PBE) and a plane-wave basis set. The VASP software package, version 5.3, was used throughout.



[Figure 4.2] Au slab with 4 layers of Au (111) surface and 10 Å vacuum gap (bottom two layers are fixed and upper two are relaxed)

4.2. Convergence test

In a plane-wave basis, the size of the basis is determined by the cut-off energy: the higher the cut-off energy, the more wave vectors are used and the more accurate the calculation. A second technical issue to be addressed is the sampling of *k* space in the first Brillouin zone. In its simplest form, Γ-point sampling (a 1 x 1 mesh) samples the energy only at $k_x = k_y = 0$. Finer *k*-meshes increase the computational demand of the calculations, but provide a more accurate sampling: where the dispersion of the bands is large (as in metals), accurate sampling becomes increasingly important. In the present calculations, where we have a large vacuum gap along the c axis, dispersion should be small so all calculations are performed with Γ-point sampling only along this axis ($k_z = 0$).

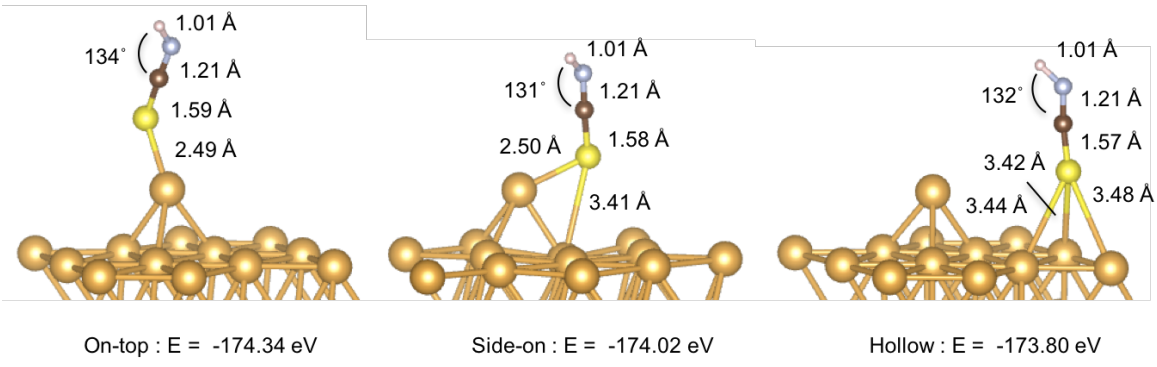
In Table 4.1, we summarise the results of convergence tests for an H-NCS molecule adsorbed at the three different sites on the unit cell (on-top, side-on and hollow). Energies (in eV) are computed with a 400 eV, 450 eV and 500 eV cut-off and a range of k-point grids from 1 x 1 to 7 x 7 respectively. In Table 4.1, all of the chemisorption sites show some common trends. Most strikingly, the energies computed with a 1 x 1 k-point mesh are ~2 eV lower energy than other meshes but from 2 x 2 onwards, the differences are much smaller, and the differences between the 2 x 2 and 7 x 7 meshes are less than 0.33 eV in all cases. In terms of the cut-off energy, the differences between 400 eV and 450 eV, 450 eV and 500 eV are minor in both case, of the order of 0.1 eV. In light of the results described in Table 4.1, we identify the 450 cut-off energy and 5 x 5 *k*-point mesh as a reasonable compromise between efficiency and accuracy, and we adopt this protocol for the remainder of this chapter.

	On-top			Side-on			Hollow		
	400 eV	450 eV	500 eV	400 eV	450 eV	500 eV	400 eV	450 eV	500 eV
1 x 1	-177.82	-177.83	-177.82	-177.68	-177.64	-177.59	-177.13	-177.24	-177.19
2 x 2	-175.57	-175.51	-175.55	-175.33	-175.30	-175.31	-174.93	-175.00	-174.89
3 x 3	-175.55	-175.52	-175.56	-175.29	-175.23	-175.32	-175.00	-174.96	-174.88
4 x 4	-175.39	-175.39	-175.43	-175.28	-175.16	-175.17	-174.83	-174.82	-174.84
5 x 5	-175.39	-175.35	-175.34	-175.24	-175.18	-175.14	-174.74	-174.72	-174.79
6 x 6	-175.24	-175.39	-175.36	-175.21	-175.23	-175.11	-174.87	-174.69	-174.72
7 x 7	-175.38	-175.41	-175.39	-175.15	-175.12	-175.10	-174.88	-174.82	-174.80

[Table 4.1] Convergence test for three possible chemisorption sites (all energies are indicated in eV)

4.3. Surface effects on the bonding of H-NCS on Au (111)

Our initial survey of the potential energy surface focusses on the simplest NCS species, H-NCS. The structures themselves are summarized in Figure 4.3 and it shows the energies of the three possible chemisorption sites, and also the structural changes caused by the surface effect. The symbol *T* refers to the on-top site where a molecule is attached on the ad-atom, *S* defines the side-on site where a molecule bridges between the ad-atom and one on the surface and *H* defines the surface site where a molecule binds in the hollow site. Of these three, the on-top structure (*T*) is clearly the most stable, followed by *S*, with adsorption into the hollow site (*H*) the least stable of the three. The latter is typically 0.32-0.54 eV less stable than the *T* global minimum, consistent with the expectation that the defect sites on the surface should be a locus for substrate binding. Molecules in the *T* and *S* isomers bond mainly to the ad-atom (Au-S ~ 2.5 Å), while at the surface site Au binds to the three Au atoms of the hollow site at similar long distances (~3.4 Å). The global stability correlates inversely with the shortest Au-S bond distance (*T* < *S* < *H*), indicating that strong Au-S binding is the major factor in lowering energy. In all three cases the geometry of the H-NCS unit is strongly bent, as it is in the free molecule, and the M-N-C angles are marginally more linear. Nevertheless, changes in the geometry of the H-NCS unit, as a whole, are rather small. The only discernible change is a small elongation of the C-S bond in the *T* and *S* isomers, suggesting a shift towards resonance structure I in Scheme 3.1. The accumulation of negative charge at sulfur in these two isomers but not in *H* is probably related to the very short Au-S bonds in *T* and *S* but not in *H*: *i.e.* strong bonding to the surface draws charge towards the sulfur.



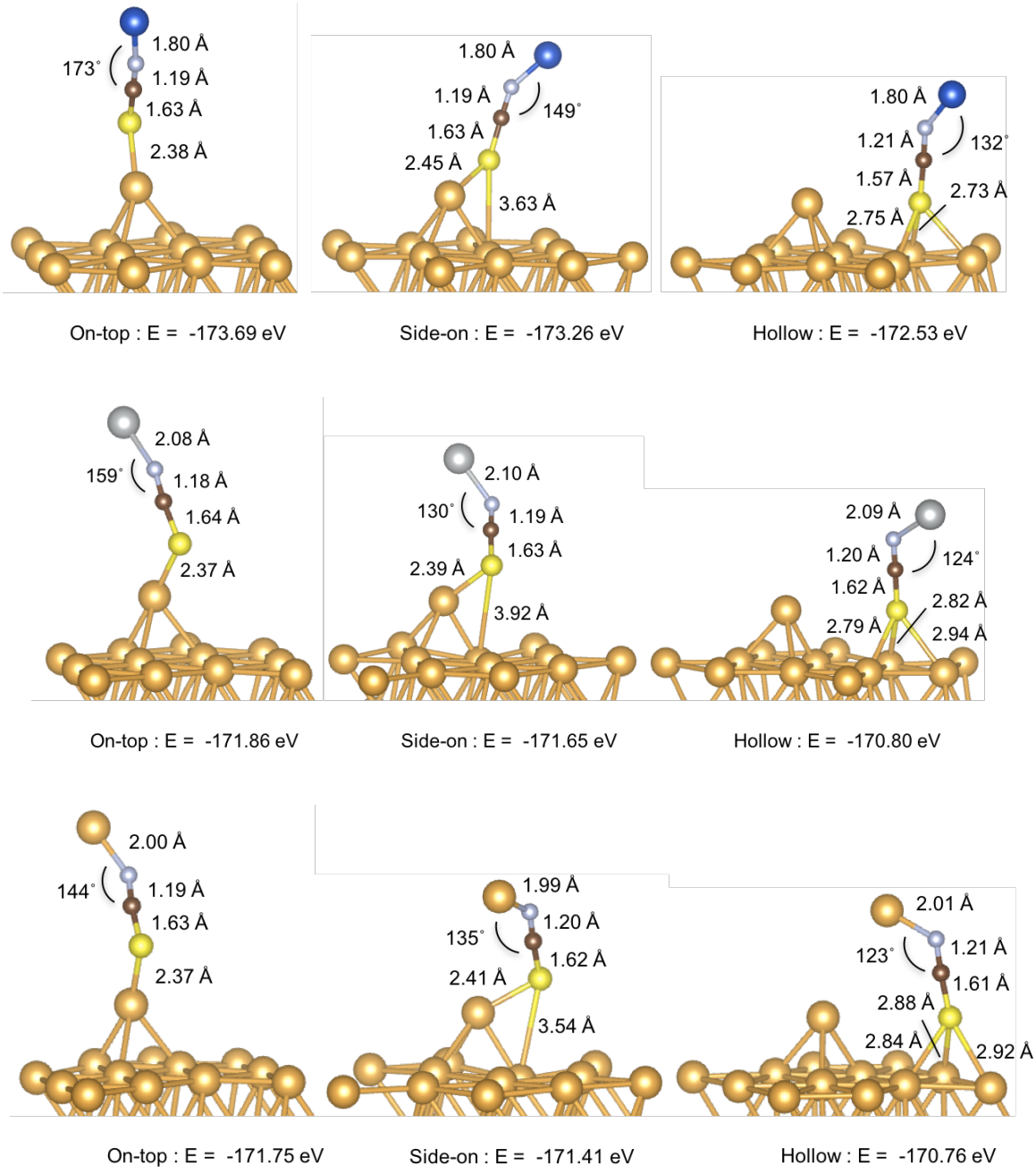
[Figure 4.3] H-NCS in on-top (*T*), side-on (*S*) and hollow (*H*) sites

4.4. Surface effects of binding of (Cu^+, Ag^+, Au^+)-NCS to Au (111)

In Figure 4.4, we show a parallel series of optimised geometries for a M-NCS unit absorbed onto the Au (111) surface, where M = Cu^+, Ag^+ and Au^+. Looking first at the copper complexes, the presence of the copper center causes some significant changes compared to the H-NCS species shown in the previous figure. The on-top (*T*) site is still the preferred site of adsorption, and the hollow (*H*) isomer is now strongly disfavored. For the most stable *T* isomer, the N-C and C-S bonds are shorter and longer, respectively, than those for the protonated species, and the Au-S bond to the surface ad-atom is contracted by 0.1 Å. The elongation of the C-S bond was already apparent in the comparison of gas-phase H-NCS and Cu-NCS (see Figures 3.2 and 3.3), but adsorption to the Au (111) surface appears to further enhance the contribution of the $N{\equiv}C\text{-}S^-$ resonance structure (form I, scheme 3.1). As a result, the C-S bond elongates 0.02 Å from gas-phase. In the *T* site the Cu-N-C unit is much closer to linear, with an angle of 173˚ (vs 134˚ in the corresponding HNCS system). The driving force for bending in Cu-NCS is in any case lower than for H-NCS (0.07 eV vs 0.14 eV, compare Figures 3.2 and 3.3) and so binding to the surface is able to exert a much greater influence in the former.

Similar features are apparent in the Ag and Au analogues, where (i) binding in the *T* isomer is preferred over *S* and very strongly over *H*, (ii) the Au-S bond lengths are much shorter in *T* and *S* and (iii) there is a distinct shift towards form I upon binding to the surface. The precise degree of bending at the M-N-C angle is very dependent on the identity of the metal, ranging from 144˚ in the Au-complex to 173˚ in the Cu-complex. We have, however, already noted that this bending mode is very soft, and so we should not attach too much significance to the precise angle at the equilibrium. The strong elongation of the C-S bond is however clear for all cases.

.

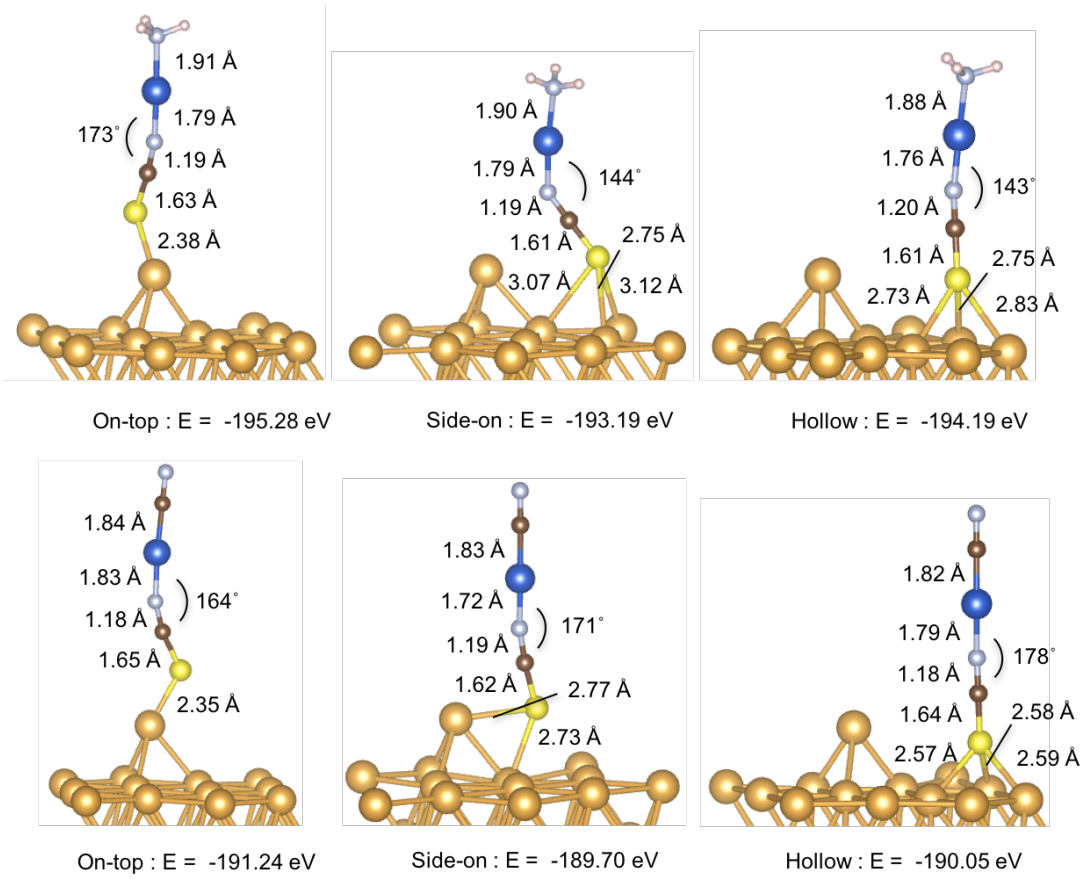


[Figure 4.4] Optimised structure and energy of M-NCS (M = Cu^+, Ag^+, Au^+) in on-top, side-on and hollow sites

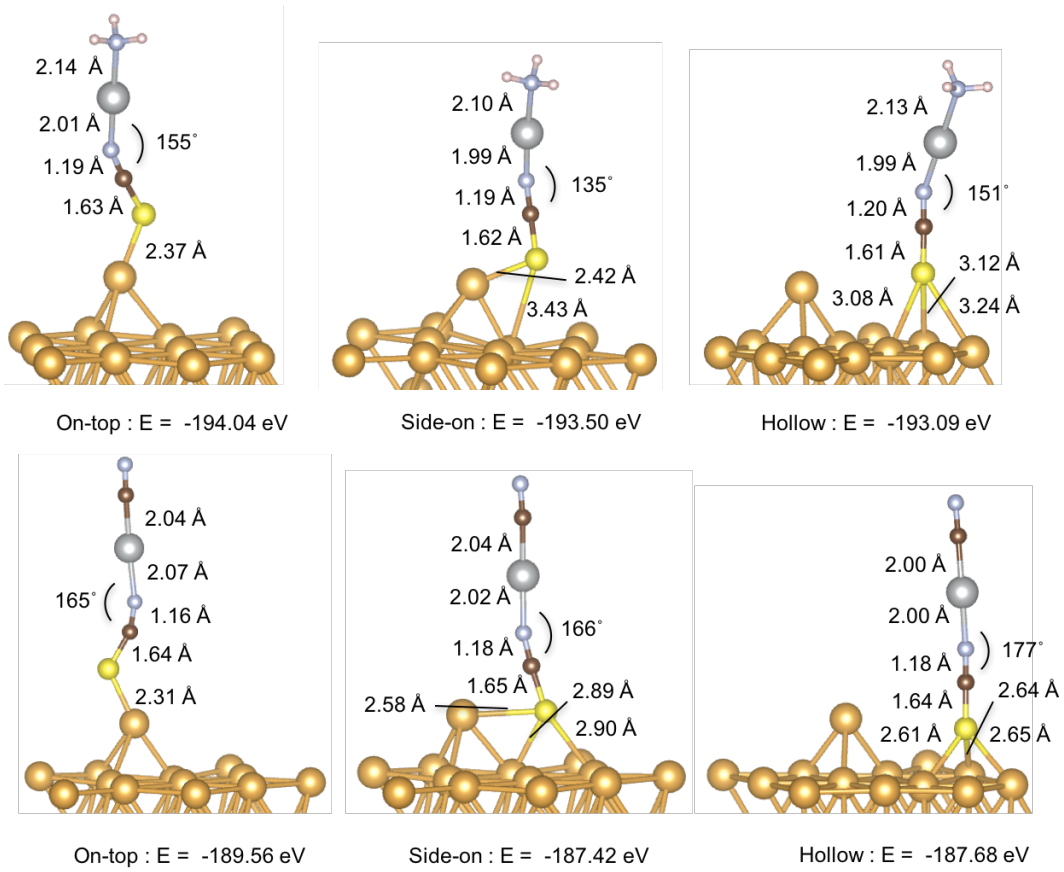
4.5. Surface effects of binding of (NH_3, CN^-)-(Cu^+, Ag^+, Au^+)-NCS to Au(111) surface

To complete this section of the thesis, we consider the influence of a trans ligand (L= NH_3, CN^-) on the binding of the L-M-NCS ligand to the surface. The optimised structures and energies for the NH_3 and CN^- capped species are compared in Figure 4.5, where again we see a clear preference for binding to the *T* site over either *S* or *H*. For the Cu species, the influence of the NH_3 ligand is minimal, as is apparent from the comparison of Figures 4.6 and 4.7. For all three metals, the binding of the NH_3 group *trans* to the NCS ligand leaves the NCS unit almost unchanged, but there is a distinct contraction of the M-NCS bond in each case. For example, whiles the H_3N-Ag-NCS and H_3N-Au-NCS bonds in the gas-phase in Figure 3.7-3.8 are 2.06 Å and 1.95 Å, the corresponding values for H_3N-Ag-NCS and H_3N-Au-NCS are 2.01 Å and 1.94 Å, respectively in *T* sites. This contraction caused by the Au surface may be because of more s/d_{z^2} hybridization on the metal centers.

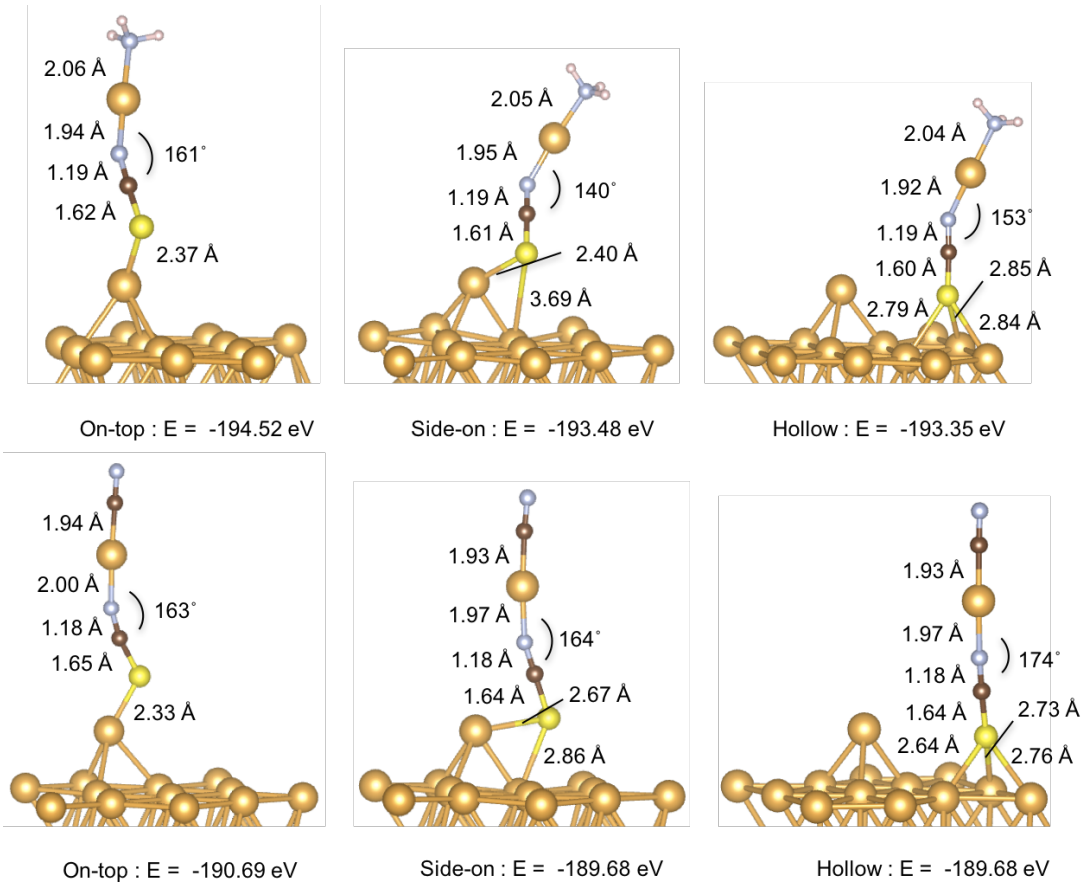
The final set of compounds that we consider here is the CN^- analogues where the electro-neutrality in the unit cell imposes a M(II) oxidation state rather than M(I). The *T* isomer is substantially unchanged from the NH_3-capped analogue, except for a small further elongation of the C-S bond (1.65 Å vs 1.63 Å). Given the increase in oxidation state, it is perhaps surprising that there is no noticeable decrease in M-NCS bond length in the NC-capped species: in fact, in the *T* isomer there is a uniform increase, with the M-N bond lengths some 0.05 Å longer in the NC-capped systems. It seems that here the very strong σ-donor characteristics of the CN^- ligand, which will cause a strong *trans* influence, outweigh the changes due to oxidation.



[Figure 4.5] Optimised structure and energy of L-Cu-NCS (L = NH_3, CN^-) in on-top, side-on and hollow sites



[Figure 4.6] Optimised structure and energy of L-Ag-NCS (L = NH_3, CN^-) in on-top, side-on and hollow sites



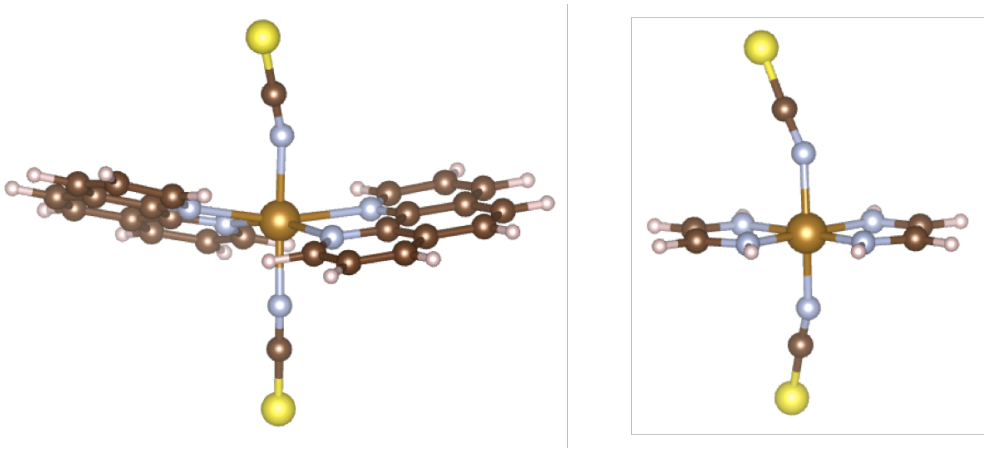
[Figure 4.7] Optimised structure and energy of L-Au-NCS (L = NH_3, CN^-) in on-top, side-on and hollow sites

4.6. Summary

In this chapter, optimised complexes in the gas-phase have been chemisorbed on an Au(111) surface, which causes substantial changes to the structural properties of NCS complexes. In general, binding at the *T* site is more stable by ~0.3-0.5 eV on H-NCS, ~0.2-1.2 eV on M-NCS and ~0.5-2 eV on L-M-NCS complexes. This indicates that molecules with greater structural complexity shows larger energetic volatility over those chemisorption sites. In addition, the Au-S bond between a molecule and gold surface tends to be shorter when the structure has a lower energy (for example, 2.3-2.4 Å in *T* site and 2.5-3.5 Å in *H* site). Finally, in terms of NCS resonance form, strong sulfur binding on Au surface, especially onto the ad-atom, causes C-S bonds to elongate. In the last chapter, we noted that complexation of NCS complexes causes an elongation of the C-S bond (C-S = 1.58 Å in H-NCS and C-S = 1.63 in NC-Cu-NCS). The surface effect from Au substrate shifts the balance of resonance even further to form I, causing further increase in the C-S bond to 1.65 Å on NC-Cu-NCS in *T* site.

5. Structure and properties of spin crossover complexes of Fe(II): $Fe(II)(phen)_2(NCS)_2$.

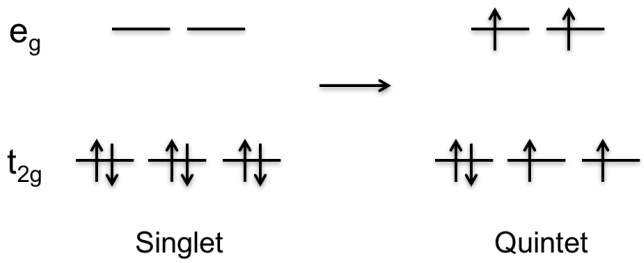
5-1. Introduction



[Figure 5.1] Left: $Fe(II)(phen)_2(NCS)_2$, right: $Fe(II)(diimine)_2(NCS)_2$

Spin crossover transition metal compounds continue to attract attention because the change in spin state causes substantial geometric changes that could, in principle, be the basis of a molecular switch.[40] This property has potential importance in the field of molecular electronics, as changing the electronic configuration may affect the conductance of the molecule.[41] The basis of spin crossover can be understood in terms of simple crystal field theory, where ideal octahedral coordination splits the d-orbitals into two degenerate subsets: triply degenerate t_{2g} and doubly degenerate e_g. The e_g orbitals are anti-bonding orbitals and lie higher in energy, separated from t_{2g} by the ligand-field splitting, Δ. The ligand-field splitting is strongly affected by the surrounding ligands at the metal center: for example, in $[Fe(II)(H_2O)_6]^{2+}$ the splitting is ~30 kcal/mol, whereas in $[Fe(II)(CN)_6]^{4-}$ it is much larger at ~94 kcal/mol.[42] The strong σ-donor and also π-acceptor properties of the CN^- ligand can increase the gap between e_g and t_{2g} orbitals substantially. The theoretical study of spin crossover compounds is challenging because the two configurations differ in the number of unpaired electrons and hence exchange energy, precisely the term which approximate density functionals seek to describe. Moreover, because the electron-electron repulsions are intrinsically large in first-row transition metals, different treatments of exchange cause large fluctuations. In the condensed phase, spin crossover can be cooperative, induceing sharp thermal spin

flips. Nevertheless, studies of the electronic structure of individual molecules have been invaluable as they offer an opportunity to study the effects of electronic and vibrational properties in detail.



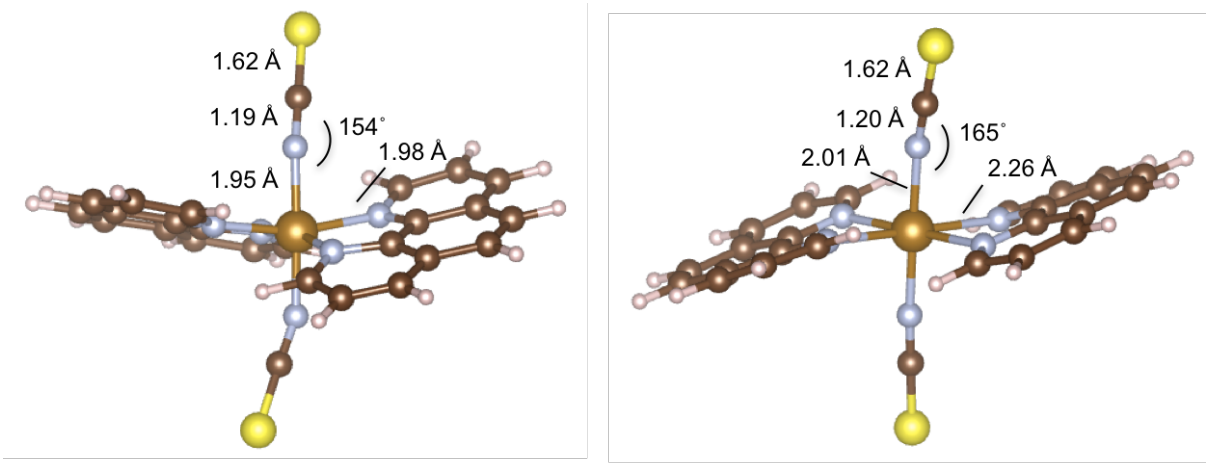
[Figure 5.2] Spin crossover orbital for Fe complex

The majority of transition metal complexes that have been studied contain Fe(II), which undergoes a transition from the singlet low-spin state to a quintet high-spin state as the temperature increased. The transition temperature occurs when the difference in Gibbs free energy, ΔG, between high and low spin states approaches zero. This is a complex problem, requiring explicit calculation of zero-point and entropic components of G, but studies of the electronic energy using DFT calculation have nevertheless been useful in establishing trends, if not absolute transition temperatures. As noted above, the calculation of spin state equilibria in transition metal complexes is very sensitive to the level of theory, and many functionals have been used for DFT calculations in this context.[43, 44] One of the earliest studies by A. X. Trautwein *et al.*[45] analyzed zero point energies of an array of Fe(II) complexes with different functionals, including the hybrid functional B3LYP and non-hybrid functionals BLYP and PW91. The results show that hybrid functionals favour high-spin states while pure gradient-corrected functionals tend to favour low-spin. This illustrates very clearly the point that the stability of Fe(II) spin crossover complexes is hugely dependant on the chosen functionals. Later, various studies confirmed that pure functionals such as BLYP, PW91 systematically favour low-spin states while hybrid functionals are in the opposite direction. To correct this effect, M. Reiher and co-workers explored a variety of hybrid functional of the B3LYP type with the amount of Hartree-Fock exchange varying from 0 to 0.24 and concludes that the optimum value is ~0.15 rather than the 0.20 used in standard B3LYP.[46,] In a more recent study, A. Ghosh *et al.* find that the newer pure functionals such as OLYP and OPBE provide better results on Fe(salen)(NO) complexes and those isomers.[47] Hybrid

functionals based on the OPBE framework have been proposed recently by Swart and co-workers, including s12h (which includes the D_3 dispersion energy along with 25% HF exchange).[48]. Later, reasonable correlations of HS–LS energy difference are also observed in OPBE functional for Fe spin crossover complexes by the Deeth group.[49]

In this chapter, a variety of functionals including PBE, OPBE, B3LYP, B3LYP*, PBE0 and s12h are examined to explore the energy gap between low and high spin states. The test compound is the Fe(II) complex $Fe(II)(phen)_2(NCS)_2$, which has been extensively studied in experimental and theoretical work. In X-ray measurements, the Fe-NCS bond lengths are 1.96 Å in the singlet and 2.06 Å in the quintet state, respectively, while the Fe-phen bond lengths are 2.00 Å in the singlet and 2.20 Å in the quintet.[50] In the subsequent study of surface effects, the span of the phen ligands will require a large unit cell and hence a large number of gold atoms. In an attempt to minimize this cost, we also consider the possibility of replacing the phen ligands with a simpler diimine model. In this chapter, we report gas-phase calculations on the isolated molecules, before moving on to surface effects in the final chapter.

5.2. Gas-phase studies on spin crossover in $Fe(II)(phen)_2(NCS)_2$



[Figure 5.3] Energy and optimised geometries of $Fe(II)(phen)_2(NCS)_2$ in two spin states

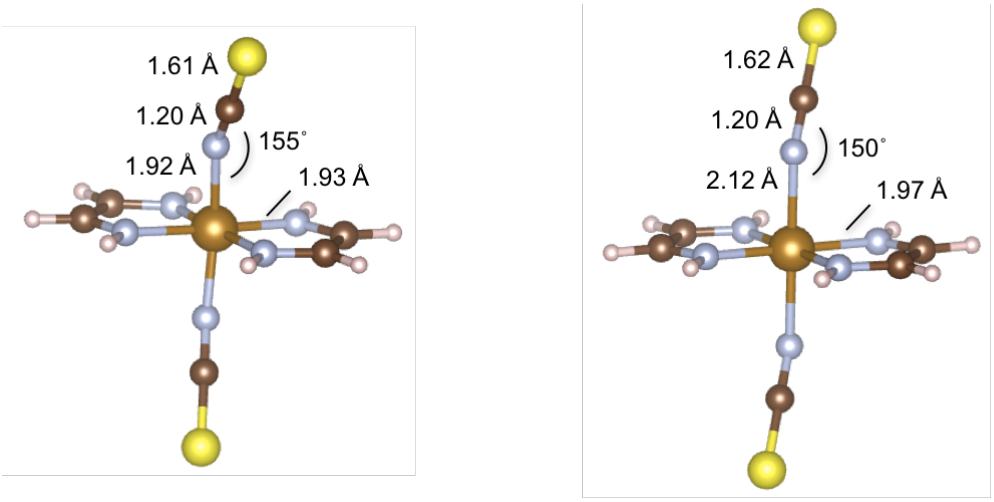
Optimised structures of $Fe(II)(phen)_2(NCS)_2$ in the singlet low-spin and quintet high-spin states are calculated using ADF software and summarized in Figure 5.3 (PBE functionl), and the key properties are collected in Table 5.1 for a variety of functionals (PBE, OPBE, B3LYP, B3LYP*, PBE0, s12H). The relative energies show that only the PBE

functional calculates the singlet spin state to be the most stable - the other five functionals indicate that the high-spin state is the lowest. With OPBE, B3LYP and B3LYP*, the energy gap is in a narrow range 0.31-0.33 eV whereas PBE0 and s12H place the gap significantly higher at 0.83 eV and 1.22 eV respectively. In PBE functional, the Fe-N bonds elongate upon transition from low-spin to high-spin states, 0.06 Å in Fe-NCS and 0.28 Å in Fe-phen bonds respectively. In theory, the spin density of the e_g anti-bonding orbitals should distribute equally over d_{z^2} and $d_{x^2-y^2}$ orbitals, but here the elongation of the Fe-phen bonds is much greater. Some of the spin density in the quintet spin state is delocalised onto the NCS^- ligands, reducing the population of d_{z^2}. This trend is apparent in all functionals: for example, the spin density on the NCS^- ligand in B3LYP is 0.12, with a 0.09 Å elongation of the Fe-NCS bond. As the Fe-NCS bond becomes longer, the communication and overlap between the N atom on NCS and Fe atom is reduced and the dominant resonance form of the NCS ligand shifts toward form I (Scheme 3.1). This trend is apparent in the Fe-N-C angles, where values lie in the range 154° to 165° for PBE, OPBE, B3LYP and B3LYP*. However, for PBE0 and s12H, the angle is substantially reduced (to 134° in s12h functional), indicating a more significant contribution from the sp^2 hybridised form. The C-S bond is relatively short compared to the L-M-NCS complexes discussed in previous chapters (1.62 Å in PBE functional), probably because the divalent Fe(II) favours resonance structure II, where the negative charge resides on the nitrogen.

		Total energy	Fe-NCS bond	Fe-phen bond	Fe spin	NCS spin	Phen spin	Fe-N-C angle	N-C bond	C-S bond
PBE	LS	-357.27	1.95	1.98	0	0	0	154	1.19	1.62
	HS	-356.11	2.01	2.26	3.67	0.36	-0.03	165	1.20	1.62
OPBE	LS	-357.59	1.92	1.96	0	0	0	161	1.19	1.61
	HS	-357.89	2.01	2.27	3.74	0.33	-0.07	171	1.19	1.61
B3LYP	LS	-407.12	1.98	2.06	0	0	0	176	1.18	1.63
	HS	-407.44	2.07	2.30	3.76	0.12	0.16	178	1.18	1.63
B3LYP*	LS	-393.27	1.97	2.04	0	0	0	173	1.18	1.63
	HS	-393.60	2.04	2.33	3.67	0.21	0.14	178	1.19	1.62
PBE0	LS	-439.27	1.95	2.02	0	0	0	176	1.18	1.63
	HS	-440.11	2.06	2.28	3.76	0.14	0.10	157	1.18	1.62
s12H	LS	-438.07	1.99	2.05	0	0	0	161	1.18	1.64
	HS	-439.29	2.12	2.32	3.77	0.13	0.10	134	1.18	1.63

[Table 5.1] Optimised structures, relative energies and spin densities for singlet and quintet states of $Fe(II)(phen)_2(NCS)_2$ with functionals, which are PBE, OPBE, B3LYP, B3LYP*, PBE0 and s12H (Total energy is valued in eV, bond length is in Å and angle is in degrees)

5.3. Gas-phase studies on spin crossover in $Fe(II)(diimine)_2(NCS)_2$



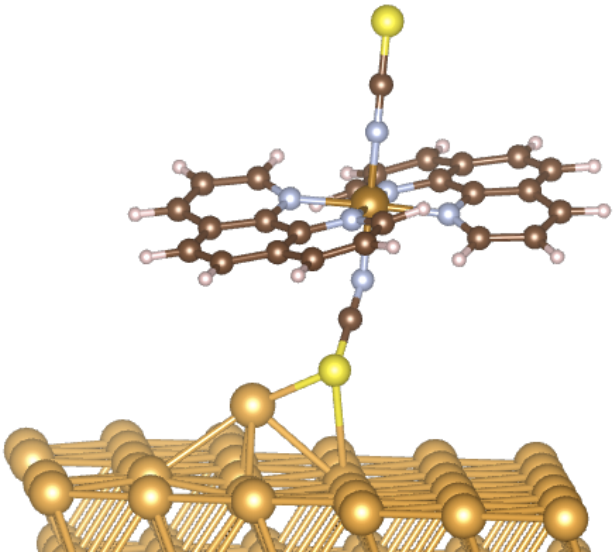
[Figure 5.4] Energy and conformational properties of $Fe(II)(diimine)_2(NCS)_2$ in two spin states (PBE functional).

In an attempt to reduce the span of the phen ligands for the subsequent periodic calculations, we have also considered the model $Fe(II)(diimine)_2(NCS)_2$ complex in low-spin (left) and high-spin (right) states. The data are summarized in Table 5.2. The energy difference between singlet and quintet states is 1.34 eV using the PBE functional, indicating a more stable singlet as observed for the full ligand. However, the OPBE and B3LYP* functionals also predicts a lower energy for the singlet spin state, by 1.15 eV, in complete contrast to the Fe-phen case. In terms of spin density, the population is now localized significantly on NCS^- and the diimine ligands (0.79-0.89 with the PBE functional), and the change in Fe-diimine bond length is very small 0.04 Å (0.28 Å in Fe-phen complex). In summary, it seems that the reduction of the ligand to a model diamine introduces low-lying ligand orbitals that substantially affect the spin crossover. On that basis, we feel that the diimine model system is not adequate for our purposes, and will not be considered further.

		Total energy	Fe-NCS bond	Fe-diimine bond	Fe spin	NCS spin	Diimine spin	Fe-N-C angle	N-C bond	C-S bond
PBE	LS	-147.54	1.92	1.93	0	0	0	155	1.20	1.62
	HS	-146.20	2.12	1.97	2.32	0.79	0.89	150	1.20	1.62
OPBE	LS	-147.66	1.90	1.90	0	0	0	155	1.19	1.61
	HS	-146.51	2.14	1.94	2.37	0.78	0.85	143	1.20	1.61
B3LYP	LS	-172.53	1.97	1.98	0	0	0	166	1.18	1.63
	HS	-172.79	2.04	2.31	3.70	0.21	0.09	175	1.18	1.62
B3LYP*	LS	-165.66	1.95	1.96	0	0	0	162	1.18	1.63
	HS	-165.55	2.04	2.26	3.73	0.24	0.03	165	1.19	1.62
PBE0	LS	-186.54	1.94	1.95	0	0	0	163	1.17	1.62
	HS	-186.96	2.04	2.27	3.75	0.17	0.08	174	1.18	1.61
s12H	LS	-185.73	1.95	1.97	0	0	0	159	1.18	1.62
	HS	-186.51	2.08	2.27	3.76	0.15	0.09	178	1.18	1.63

[Table 5.2] Optimiezd structures, relative energies and spin densities for singlet and quintet states of $Fe(II)(diimine)_2(NCS)_2$ with functionals, which are PBE, OPBE, B3LYP, B3LYP*, PBE0 and s12H (Total energy is valued in eV, bond length is in Å and angle is in degrees)

5.4 Influence of surface binding on the spin-crossover in $Fe(II)(phen)_2(NCS)_2$



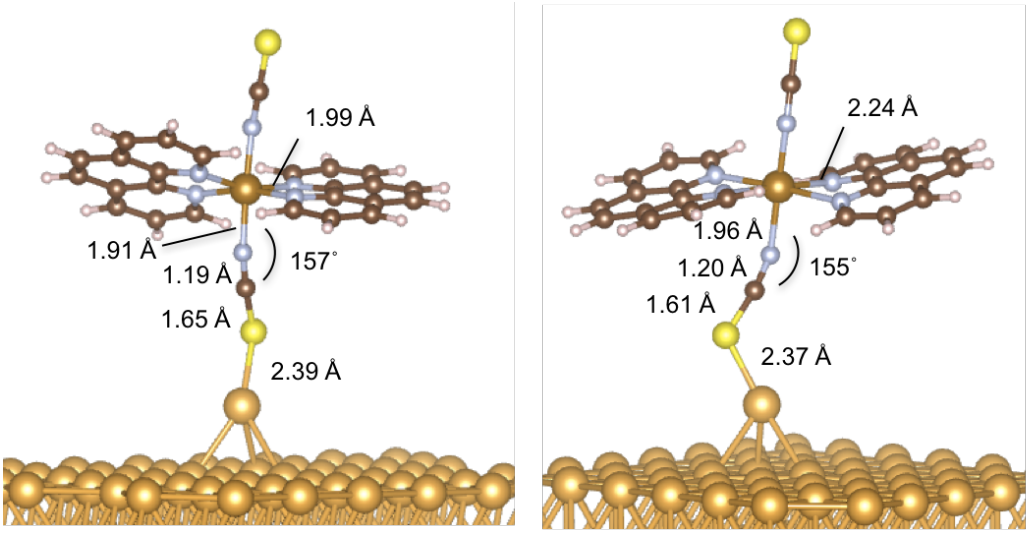
[Figure 5.5] Fe-phen molecule on Au (111) surface in side-on site

It is well known that the electronic states of spin-crossover compounds can be changed by external stimuli such as light, pressure, magnetic or electric fields. The conductance is also strongly affected, and is measurable through Scanning Tunneling Microscopy. It is therefore important to establish the extent to which adsorption on a surface affects the spin-crossover equilibrium.[51] In the case of a single molecule chemisorbed on metallic surfaces, strong hybridization can affect the conformational structure of the molecule, and hence the ligand-field splitting between the e_g and t_{2g} orbitals. Binding to an Au(111) surface has been shown to cause conformational change on self-assembled monolayers and similar factors may influence the electronic properties of $Fe(II)(phen)_2(NCS)_2$. The chemical interaction between the molecule and the gold layer may either reduce or increase the strength of bonding between the central metal and surrounding ligands, altering the balance between the two magnetic states. In contrast to the numerous gas-phase computational studies that have been performed, studies on the spin crossover phenomenon in complexes chemisorbed on Au(111) using ab-initio DFT methods are limited in number. S. Lebegue *et al.* have explored the electronic properties of $Fe(phen)_2(NCS)_2$ as a single molecule with the GGA + U method taking explicitly into account the periodicity of the crystal.[52] They have

found that the low-spin state is favored at low temperature and high-spin at high temperature, but the identity of the ground state is dependent on the value of *U*, with the two states almost degenerate between *U* = 2.5 and 3.5. This work highlights the importance of magneto-elastic coupling in controlling spin cooperativity. Another significant study was conducted by S. Gueddida and M. Alouani in 2013, who analyzed the $Fe(phen)_2(NCS)_2$ molecule absorbed on a Cu (001) substrate with a nitrogen monolayer.[53] They showed that the adsorption on the substrate reduces drastically the molecule-surface adsorption energy and chemical bonding, making the molecule switchable between its two magnetic states.

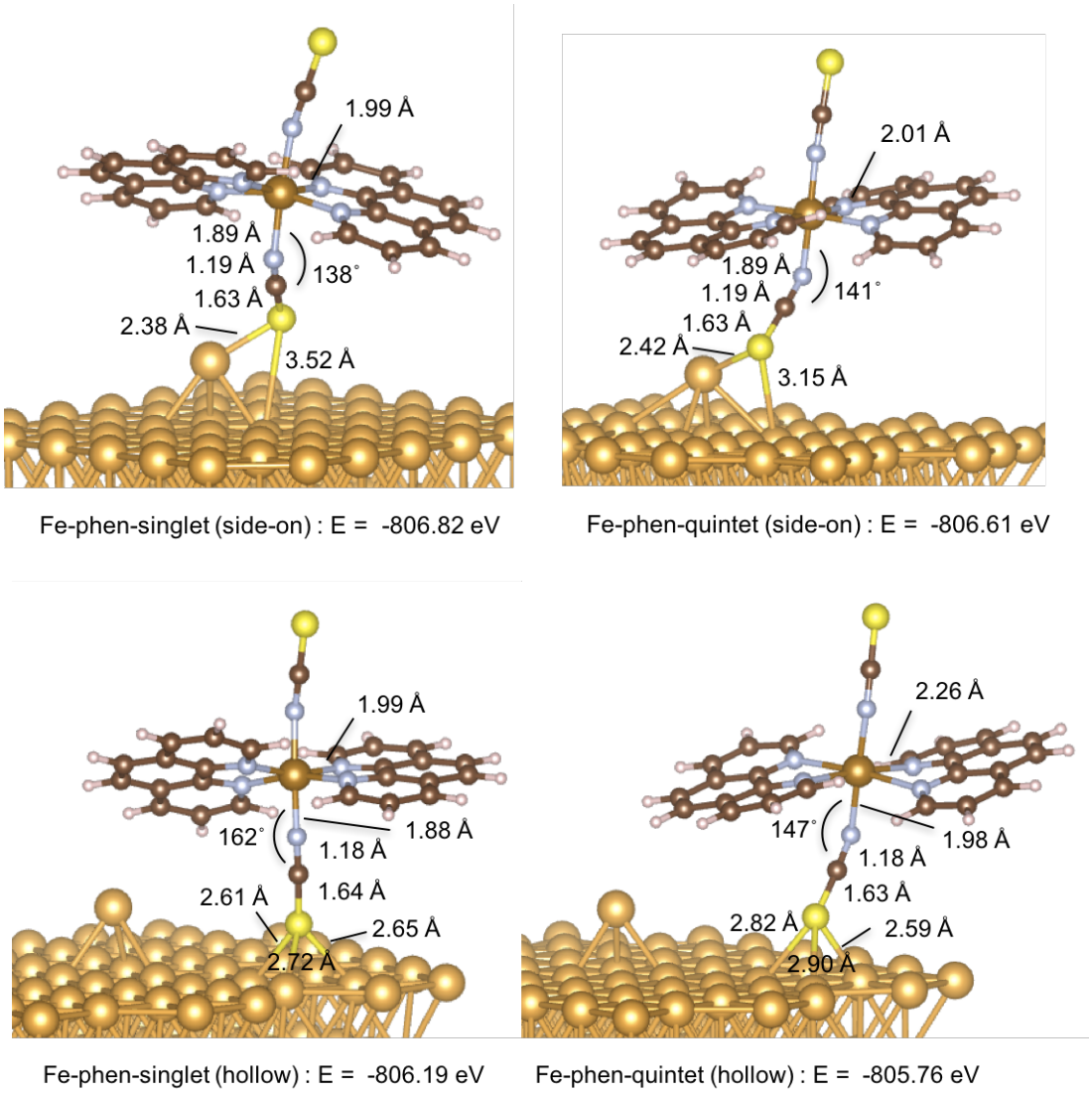
In this section, we explore surface effects on $Fe(II)(phen)_2(NCS)_2$ complexes chemisorbed on Au(111) substrates. The same chemisorption sites (on-top, side-on and hollow sites) considered in the study of simple NCS adducts are included, following motivation from the study by J. Gottschalck and B. Hammer.[25] Optimised structures from a gas-phase calculation using the PBE functional are grafted onto the Au(111) surface and re-optimised in periodic system, also with the PBE functional. The calculations have been performed using the VASP software with a plane wave cut off of 450 eV and a 5 x 5 x1 k-point grid. These settings were tested for convergence in chapter 4. The Au(111) surface is modelled by four atomic layers, the lower two of which are fixed and the upper two are relaxed. One ad-atom is attached on the surface to simulate surface defects, creating three possible chemisorption sites for octahedral complexes. The vacuum slab is extended to 15 Å from 10 Å to accommodate the greater height of the molecule, and a 6 x 6 extension of the normal hexagonal unit cell in the a and b directions is used rather than a 3 x 3 extension to accommodate the greater span of the molecule compared to linear L-M-NCS. We explore the energy difference between low and high spin states of $Fe(phen)_2(NCS)_2$ as well as the spin density at the three possible chemisorption sites to understand how various chemisorption sites affect the stability and spin states of those complexes. Finally, the influence of the choice of Hubbard *U* is examined using various values (*U* = 0.0, 1.5, 2.5, 3.5).

Figure 5.6 summarizes the chemisorbed structure of singlet (left) and quintet (right) states at the three possible sites, on-top (*T*), side-on (*S*) and hollow (*H*) (PBE functional, U = 0). Table 5.3 summarizes the spin densities for the central Fe metal and the NCS^- and phen ligands. At the PBE level with U = 0, the most stable structure is again the *T* site, which, in the singlet state, is lower in energy by 0.13 eV and 0.76 eV compared to the *S* and *H* sites, respectively. This trend is similar to that identified for the chemisorption of linear complexes in chapter 4, which suggests that the preference of chemisorption site for NCS-capped complexes is not strongly affected by the identity of the metal atom or the other ligands. This suggests that it could be a locus of molecule around the ad-atom in the process of chemisorption when SAMs are formed on the surface. Less stable high-spin states have been located only for the *T* and *H* site, where the spin densities are 3.56 and 3.53 respectively. For the S site, all attempts to locate a high-spin minimum failed, the system converging back to a closed-shell state with no spin density. One possible explanation for this is that the bonding between the Au surface and the NCS ligand strengthens the Fe-NCS bond and so increases Δ - it is notable that the optimised Fe-N bond of 1.89 Å is significantly shorter than the gas-phase value of 1.95 Å. The contraction of the M-NCS bonds in the surface calculations compared to the gas-phase is in fact a general observation, and was also apparent in the linear L-M-NCS (L = NH_3, CN^-) complexes, possibly related to the stronger Au-S π bonding.



Fe-phen-singlet (on-top) : E = -806.95 eV

Fe-phen-quintet (on-top) : E = -806.57 eV



[Figure 5.6] $Fe(phen)_2(NCS)_2$ with singlet (left) and quintet (right) spin states in three possible sites (on-top: upper, side-on: middle and hollow: bottom)

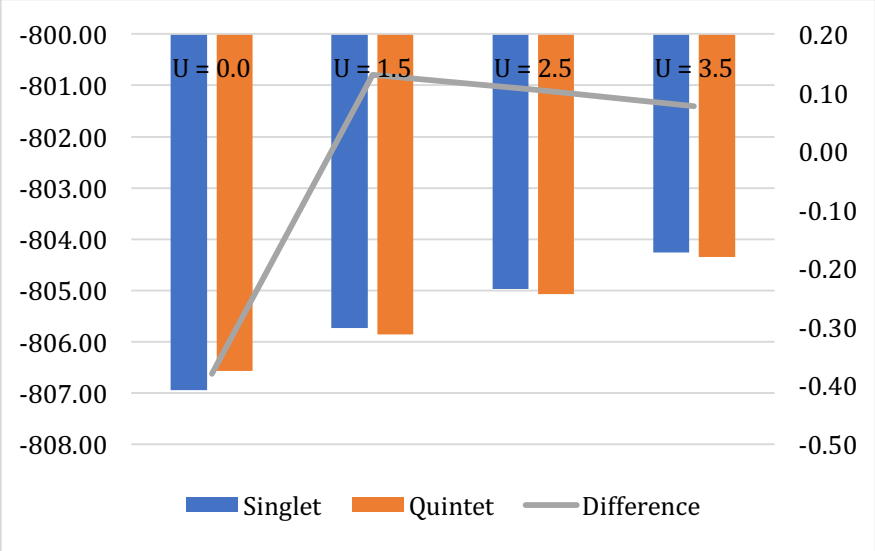
	Fe spin	NCS spin	Phen spin
On-top	0.00	0.00	0.00
	3.56	0.21	0.14
Side-on	0.00	0.00	0.00
	0.00	0.00	0.00
Hollow	0.00	0.00	0.00
	3.53	0.22	0.16

[Table 5.3] Spin density of Fe atom and each ligand (NCS^- and phen) for three sites

In the gas-phase calculation, a variety of functionals (B3LYP, B3LYP*, s12h, PBE0) were used that differs in the amount of Hartree Fock exchange. The relative energies of spin states depend strongly on the balance between the repulsion of opposite-spin electrons and the ligand-field splitting between e_g and t_{2g} orbitals. Hybrid functionals generally overestimate the stability of high spin state while GGA functionals do the opposite. In periodic systems, similar features are introduced through the Hubbard *U* method, which adds an energetic penalty for double occupation of an orbital. Larger values therefore tend to favor high-spin configurations. Table 5.4 shows the relative energies of singlet and quintet states of the Fe-phen complex on the *T* site (the most stable chemisorption site for Fe-phen complex) for a range of *U* values (*U* = 0.0, 1.5, 2.5, 3.5). As noted above the energy difference between singlet and quintet is 0.38 eV when *U* = 0.0 but for *U* = 2.5, the ordering is reversed with the quintet lower by 0.11 eV. These numbers are much smaller in comparison with those in gas-phase, where PBE places the singlet 1.15 eV below the singlet. This suggests that Au surface chemisorption reduces the spin-crossover energy, as suggested by S. Gueddida and M. Alouani, who found that chemisorption of $Fe(phen)_2(NCS)_2$ on a metal surface make those complexes more switchable from low to high spin states and *vice versa*.

	U = 0.0	*U* = 1.5	*U* = 2.5	*U* = 3.5
Singlet	-806.95	-805.73	-804.97	-804.27
Quintet	-806.57	-805.87	-805.08	-804.34

[Table 5.4] Global minimum energies for Fe-phen complex in on-top site with a range of *U* values (*U* = 0.0 to 3.5)



[Figure 5.7] Chart of global minimum energies for Fe-phen complex in on-top site with a range of *U* values (*U* = 0.0 to 3.5)

5.5. Summary

In this chapter, two complexes, Fe(II)$(phen)_2(NCS)_2$ and Fe(II)$(diimine)_2(NCS)_2$ have been optimised in the gas-phase using different functionals. For Fe(II)$(phen)_2(NCS)_2$, the singlet spin state is stabilized below the quintet state only by the PBE functional (by 1.15 eV). On the other hand, hybrid functionals (B3LYP, B3LYP*) stabilize the quintet by ~0.3 eV, as does the OPBE functional. The remaining two functionals, PBE0 and s12H, show a much greater stabilisaton of the high-spin state, which is 0.8/1.2 eV more stable at this level. Spin density is localized more on the Fe atom with the hybrid functionals whereas in non-hybrid functionals, ~0.3 of an electron is delocalized onto the NCS ligand. In terms of structure, The Fe-NCS and Fe-phen bond lengths increase by ~0.1 Å and ~0.25 Å upon increase in spin state, in reasonable agreement with the experimental values of 0.1 Å and 0.2 Å. Finally, attempts to reduce the size of complexes by replacing phen with a model diimine failed because large amounts of spin density accumulate on the NCS and diimine ligands, suggesting that the vacant orbitals on the latter are too low in energy.

When attached to an Au(111) surface we find that binding to the *T* site is still the most favorable, just as it was for the linear complexes studied in Chapters 3 and 4. The *T* site is favored by ~0.8 eV over others, and this trend is independent of spin state. With the PBE functional and a Hubbard *U* value of 0, the singlet is stable by ~0.4 eV at both the *T* and *H* sites, mirroring the trend in the gas-phase calculations with the same functional although the energetic separation of the spin states is smaller. When the *U* value increases to 2.5, the relative stability of the spin states is inverted, with the quintet more stable by 0.11 eV. Thus just as the position of the spin-crossover equilibrium is strongly dependent on the amount of Hartree-Fock exchange in the functional, it is also strongly dependent on the Hubbard *U* value.

6. Conclusion

In Chapters 4 to 6, we have analyzed the nature of the bonding of the NCS ligand to a range of atoms and groups (H-NCS, M-NCS (M =Cu^+, Ag^+, Au^+) L-M-NCS (L = NH_3, CN^-) and $Fe(phen)_2(NCS)_2$, both in the gas phase and when attached to an Au(111) surface. In the latter case, we have considered three possible chemisorption sites (on-top, side-on and hollow), and found that the on-top site, where the molecule is bound to a single ad-atom on the surface, is energetically preferred. The degree of bending of the M-N-C bond is a useful indicator of hybridisation at the nitrogen, but the bending mode is soft and difference between the linear and substantial deviations in the angle cost only 0.1-0.4 eV. We can interpret the changes in computed structure of the NCS ligand in terms of a continuum of structures lying between two limiting resonance structures of NCS, one with an N≡C triple bond, the other with N=C and C=S double bonds (scheme 3.1). Complexation of the NCS ligand causes an elongation of the C-S bond from 1.57 Å in H-NCS to ~1.64 Å in L-M-NCS. Binding to an Au surface causes a further 0.01-0.02 Å increase in C-S bond length. In the Fe(II) complex, the C-S bond length is rather shorter at ~1.62 Å because the higher oxidation state favours the accumulation of negative charge at nitrogen and hence tips the balance towards the $^-$N=C=S resonance form. Upon chemisorption, binding to the on-top site (T) is the most stable in all cases, and the stability of the complexes correlates with Au-S bond lengths (a shift to resonance form I with a negative charge at S). The lower the energy on the surface, the shorter of Au-S bond between the surface and molecule; 2.3-2.5 Å in the on-top site and 2.5-3.5 Å in the hollow site.

The separation between singlet and quintet states in $Fe(phen)_2(NCS)_2$ varies considerably with functional. The OPBE functional provides a reasonable description of the spin crossover behaviour in the complex, with a 0.3 eV energy gap and 0.1 Å and 0.2 Å elongation of the Fe-NCS and Fe-phen bonds, respectively. Chemisorption on an Au(111) surface shifts the spin crossover equilibrium: for the PBE functional a 1.15 eV preference for the low-spin state becomes 0.4 eV on the surface. The choice of Hubbard *U* in the periodic calculations has a similar impact to the amount of Hartree Fock exchange in the

gas-phase calculations - larger values of *U* systematically favour the high-spin state.

7. References

[1] D. Kahng, *United States Patent Office*, 1963, 3102230.

[2] G. E. Moore, *Proceedings of the IEEE*, 1998, **86**, 1.

[3] T. Bradshaw, *Financial Times*, 2015, July 16.

[4] E. Lörtscher, *Nat. Nanotechnol.*, 2013, **8**, 381.

[5] J. C. Cuevas and E. Scheer, Molecular Electronics, *World Scientific*, 2010.

[6] S. Molen, R. Naaman, E. Scheer, J. Neaton, A. Nitzan, D. Natelson, N. Tao, H. Zant, M. Ruben, M. Mayor, M. Reed and M. Calame, *Nat. Nanotechnol.*, 2013, **8**, 385.

[7] E. Lörtscher, *Nat. Nanotechnol.*, 2013, **8**, 377.

[8] N. Baadji and S. Sanvito, *Phys. Rev. Lett.*, 2012, **108**, 217201.

[9] B. Mann and H. Kuhn, *J. Appl. Phys.*, 1971, **42**, 11.

[10] A. Aviram and M. A. Ratner, *Chem. Phys. Lett.*, 1974, **29**, 2.

[11] D. Sekulić and M. Živanov, Electronics, 2010, **14**, 2.

[12] M. Ratner, *Nat. Nanotechnol.*, 2013, **8**, 378.

[13] G. Binning and H. Rohrer, *Phys. Rev. Lett.*, 1982, **49**, 57.

[14] S. V. Aradhya and L. Venkataraman, *Nat. Nanotechnol.*, 2013, **8**, 399.

[15] N. J. Tao, *Nat. Nanotechnol,* 2006, **1**, 173.

[16] S. M. Peng, C. Wang, Y. Jang; Y. Chen, F. Li, C. Mou and M. Leung, *J. Magn. Magn. Mater.*, 2000, **209**, 80.

[17] F. A. Cotton, D. Chae, J. F. Berry, S. Jung, C. A. Murillo and Z. Yao, *J. Am. Chem. Soc.*, 2006, **39**, 3065.

[18] C. B. Gorman, R. A. Wassel, R. Fuierer and N. Kim, *Nano Lett.*, 2003, **3**, 1617.

[19] S. M. Lindsay, G. K. Ramachandran, T. J. Hopson, A. M. Rawlett, L. A. Nagahara and A. Primak, *Science*, 2003, **300**, 1413.

[20] P. S. Weiss, Z. J. Donhauser, B. A. Mantooth, K. F. Kelly, L. A. Bumm, J. D. Monnell, J. J. Stapleton, D. W. Prince Jr, A. M. Rawlett, D. L. Allara and J. M. Tour, *Science*, 2003, **292**, 2303.

[21] I. Chen; M. Fu, W. Tseng, J. yu; S. Wu, C. Ku; C. Chen and S. Peng, *Angew. Chem. Int. Ed.*, 2006, **45**, 5814.

[22] M.S. Alam, M. Stocker, K. Gieb, P. Muller, M. Haryono, K. Student and A. Grohmann, *Angew. Chem. Int. Ed.*, 2010, **49**, 1159.

[23] D. Aravena and E. Ruiz, *J. Am. Chem. Soc.*, 2012, **134**, 777.

[24] H. Gronbeck, W. Andreoni and A. Curioni, *Int. J. Quantum Chem.*, 2000, **80**, 598.

[25] J Gottschalck and B. Hammer, *J. Chem. Phys.*, 2002, **116**, 784.

[26] G. Brocks, D. Otaĺvaro and T. Veening, *J. Phys. Chem. B*, 2012, **116**, 7826.

[27] J. Letard, C. Balde, C. Desplanchesa and O. Nguyen, *J. Phys.*, 2009, **148**, 012026.

[28] M. Gruber, T. Miyamachi, V. Davesne, M. Bowen, S. Boukari, W. Wulfhekel, M. Alouani and E. Beaurepaire, *J. Chem. Phys.*, 2017, **146**, 092312.

[29] G. te Velde, F. M. Bickelhaupt, E. J. Baerends, C. Fonseca-Guerra, S. J. A. Gisbergen, J. G. Snijders and T. Ziegler, *J. Comput. Chem.*, 2001, **22**, 931.

[30] C. Fonseca-Guerra, J. G. Snijders, G. Vede and E. J. Baerends, *Theor. Chem. Acc.*, 1998, **99**, 391.

[31] G. Kresse and J. Furthmüller, *Comput. Mater. Sci.*, 1996, **6**, 15.

[32] J. P. Perdew, K. Burke and M. Ernzerhof, *Phys. Rev. Lett.*, 1996, **77**, 3865.

[33] G. Kresse and D. Joubert, *Phys. Rev. B*, 1999, **59**, 1758.

[34] L. P. Walters and F. M. Bickelhaupt, *Open Chem.*, 2013, **2**, 106.

[35] S. A. Carvajal, J. J. Novoa and S. Alvarez, *J. Am. Chem. Soc.*, 2004, **126**, 1465.

[36] W. A. Sokalski, *Chem. Phys. Lett.*, 1983, **98**, 86.

[37] B. A. McGuire, M. Martin-Drumel, S. Thorwirth, S. Brünken, V. Lattanzi, J. L. Neill, S. Spezzano, Z. Yu, D. P. Zaleski, A. J. Remijan, B. H. Pate and M. C. McCarthy, *Phys. Chem. Chem. Phys.*, 2016, **18**, 22693.

[38] T. Custer, M. Gronowski, M. Turowsk and R. Kolos, *Theor. Chem. Acc.*, 2016, **135**, 222.

[39] H. Häkkinen**,** *Nat. Chem*., 2012, **4**, 443.

[40] P. Gütlich; A. Hauser and H. Spiering, *Angew. Chem. Int. Ed.*, 1994, **33**, 2024.

[41] E. Ruiz, Phys. Chem. Chem. Phys., 2014, **16**, 14.

[42] J. McCleverty, Chemistry of the First-row Transition Metals, Oxford university Press, 1990.

[43] A. Fouqueau, M. E. Casida, L. Daku, A. Hauser, F. Neese, *J. Chem. Phys.*,2005, **122**, 044110.

[44] S. Ya and F. Neese, *Inorg. Chem. Commun.*, 2010, **49**, 772.

[45] A. X. Trautwein, H. Paulsen, L. Duelund, H. Winkler and H. Toftlund, *Inorg Chem* , 2001, **40**, 2201.

[46] M. Reiher, *Inorg Chem*, 2002, **41**, 6928.

[47] J. Conradie and A. Ghosh, *J. Phys. Chem. B*, 2007, **111**, 12621.

[48] M. Swart, *Chem. Phys. Lett.*,2013, **580**, 166.

[49] B. J. Houghton and R. J. Deeth, *Eur. J. Inorg. Chem.*, 2014, 4573.

[50] P. Gultich and H. A. Goodwin, Spin crossover in transition metal compound III, *Springer*, 2004.

[51] S. Gueddida and M. Alouani, *Phys. Rev. B*, 2013, **87**, 144413.

[52] S. Lebegue; S. Pillet and J. G. Angyan, *Phys. Rev. B*, 2008, **78**, 024433.